CONSERVED NUCLEAR MORPHOLOGY IDENTIFIES FUNCTIONAL RADIAL GLIA NEURAL PROGENITORS

Authors: Soriano J.P.[1,2], Borau C.[3,4], Sortino R.[5,6], Garma L.[7], Ortega J.A.[1,2], Asín J.[8], Alcántara S.[1,2,*]

Affiliations:

[1] Department of Pathology and Experimental Therapeutics, Institute of Neurosciences, University of Barcelona, L'Hospitalet de Llobregat, Barcelona 08907, Spain.

[2] Neurodevelopmental Disorders Group, NeuroBell, Institut d'Investigació Biomèdica de Bellvitge (IDIBELL), L'Hospitalet de Llobregat, Spain.

[3] Centro Universitario de la Defensa de Zaragoza, Zaragoza, 50090, Spain.

[4] Multiscale in Mechanical and Biological Engineering (M2BE), Mechanical Engineering Dept, University of Zaragoza, Zaragoza, Spain.

[5] Institute for Bioengineering of Catalonia (IBEC), The Barcelona Institute of Science and Technology, Carrer de Baldiri Reixac, 10-12, 08028, Barcelona, Spain.

[6] CIBER-BBN, ISCIII, Carrer de Melchor Fernández Almagro, 3, 28029, Madrid, Spain.

[7] Centro Nacional de Investigaciones Oncológicas–CNIO, Melchor Fernández Almagro 3, Madrid, 28029, Spain.

[8] Department of Statistical Methods, University of Zaragoza, Zaragoza, Spain.

SUMMARY (150 words)

Radial glia (RG) progenitor cells are the principal neural progenitors of the embryonic brain, giving rise to neurons and glial cells. RG apical-basal polarity and anchorage are crucial for maintaining their integrity and function. By using a biomimetic substrate that reproduces RG surface properties and mechanical anisotropy, we previously described the dedifferentiation of cultured astrocytes into functional RG, although the underlying mechanotransducive components remain largely unknown. Here we analyzed the role of nuclear morphology in mechanically driven RG induction, as nuclear deformation is critical for driving gene expression and cell fate changes in response to mechanical signals. A multivariate logistic regression model developed for fitting RG probability revealed the existence of intrinsic nuclear constraints, allowing a precise range of permitted RG nuclear morphologies, which are associated with calcium dynamics and conserved *in vivo*, *in vitro* and through evolution. Moreover, nuclear deformation predicts astrocyte or RG fate acquisition in response to mechanical signals.

Keywords

RG niche biomimetic material, statistical modeling, neural development, nuclear mechanobiology, calcium imaging

INTRODUCTION

During embryonic development, biochemical and mechanical cues from the microenvironment shape neural tube formation and control neural progenitors' proliferation, functional properties and fate decisions [1-3]. Radial glia (RG) are the principal neural progenitors that generate neurons and glial cells, directly or through transit amplifying intermediate progenitors (IP) [4,5]. RG are bipolar cells spanning the cerebral wall from the ventricular (apical) to the pial (basal) surfaces. Apical-basal anchorage generates mechanical tensions and localized exposure to extracellular and mechanical signals, which are key for maintaining nuclear interkinetic migration during cell cycle, RG integrity and function, including serving as scaffolds for neuronal migration. Detachment from the ventricle or the pia while retaining apical-basal polarity generates outer RG (oRG) or truncated RG (tRG) respectively, which maintain self-renewing potential [3]. On the contrary, complete detachment generates nonpolar IP expressing T-box transcription factor TBR2/EOMES (TBR2) [6], neural/glial antigen 2 (NG2) proteoglycan [7], or GS Homeobox 2 transcription factor (GSX2) [8], which exhibit different fate potentiality. Finally, RG directly transforms into astrocytes at the end of neurogenesis [9]. These developmental transitions seem to occur via a transcriptional continuum, and frequently, cells assume their final fate post-mitotically by non-cell autonomous environmental factors [10 3]. Importantly, astrocyte is not a terminal state, and the differentiation can be partially reverted into RG-like progenitors after a lesion [10]. In fact, a subgroup of astrocytes expressing glial fibrillary acidic protein (GFAP) and SRY-box transcription factor 2 (Sox2) were recently identified as quiescent adult neural stem cells (NSC) with neurogenic capacity, characteristics shared with their RG embryonic counterparts [11].

Biomaterial strategies mimicking the physical characteristics of the tissue *in vivo* have been used for mechanobiology studies analyzing the effects of niche mechanical cues on NSC differentiation [12,13]. Using a non-degradable micro3D RG biomimetic material, we have previously demonstrated an essential role of local physical constraints in inducing astrocyte transformation into functional RG, which adopt bipolar morphology, express paired box 6 (Pax6) and Sox2 transcription factors and support neuronal migration [14,15]. Ln2PMMA is a synthetic scaffold of poly (methyl methacrylate) (PMMA) with 2μm linear grooves that mimic RG topology, and the hydrophobicity and negative charge of RG plasma membrane. Both topology and surface properties are essential, as thicker anisotropic topographies (5-20μm), flat PMMA, or hydrophilic and positively charged substrates as chitosan, even with 2μm groove topographies, failed to induce functional RG [14,16]. These results highlight that biophysical signals mimicking surface properties and topology of the RG embryonic niche are sufficient to induce some RG

functional phenotypes. However, the mechanosensing and mechanotransducive mechanisms underlying this process are largely unknown.

Mechanotransduction is the conversion of mechanical forces generated by the microenvironment into biochemical signals and cellular responses [17]. Mechanosensitive channels and cell adhesion proteins in the cell membrane generate tensions through the cytoskeleton that translate environmental mechanical signals to the nucleus. Subsequent nuclear deformation, changes in nuclear envelope composition and chromatin remodeling are critical in translating these external mechanical signals into changes in gene expression and cell fate/behavior [18-20]. For example, mechanosensitive cation channels and calcium dynamics regulate the proliferative capacity of neural progenitors [21,22], centrosome anchoring to the apical membrane regulates RG mechanical properties affecting their proliferative and neurogenic capacity [23] , and nuclear deformation is essential for the interkinetic nuclear migration in RG [24]. Moreover, nuclear morphology can be used as cell state marker for senescence and malignancy [25]. Altogether, changes in nuclear morphology have the potential for becoming a powerful tool to forecast cell state and fate.

Here, we sought to investigate the role of nuclear morphology in RG induction and functional maintenance using the previously described RG mimetic substrate ln2PMMA. We found that nuclear deformation and changes in nuclear lamina composition precede the mechanical induction of RG markers expression. Additionally, by statistically correlating nuclear features with gene expression, we revealed the existence of intrinsic RG nuclear constraints and a precise range of permitted RG nuclear morphologies, which are associated to physiological parameters conserved *in vivo* and through evolution.

RESULTS

Ln2PMMA changes the nuclear morphology of Astrocyte – RG lineage cells

We inquired whether changes in nuclear morphology were associated with changes in cell-type markers expression (increased Pax6/Sox2 and decreased GFAP expression) during ln2PMMA mechanical RG induction, as nucleus-cytoskeletal network coupling modulates nuclear shape, chromatin organization and gene transcription [19,26,27]. To address this, we grew astrocyte-enriched cultures on ln2PMMA and flat borosilicate glass (control) substrates for 3 days in vitro (3DIV) (**Figure 1A**). A total of 3855 cells, 2135 in control and 1720 in ln2PMMA were analyzed, and nuclear morphology

parameters (area and eccentricity) of Hoechst stained nuclei were associated to their cell-type markers expression, using a custom-made MATLAB algorithm (see material and methods, **Figure 1B**). To label different cell types across glial lineage we used the intermediate filaments GFAP for astrocytes and nestin for immature astrocytes/RG, the proteoglycan NG2 for intermediate oligodendrocyte progenitors (OPC), the transcription factors Sox2 for NSC, Pax6 for RG, and Gsx2 for tripotential intermediate progenitors (**Figure 1C**). At 3DIV, the proportion of GFAP+ astrocytes was significantly reduced while Pax6+ RG was significantly increased in ln2PMMA with respect to control (**Figure 1D**), consistent with the RG induction by ln2PMMA previously described [14,15].

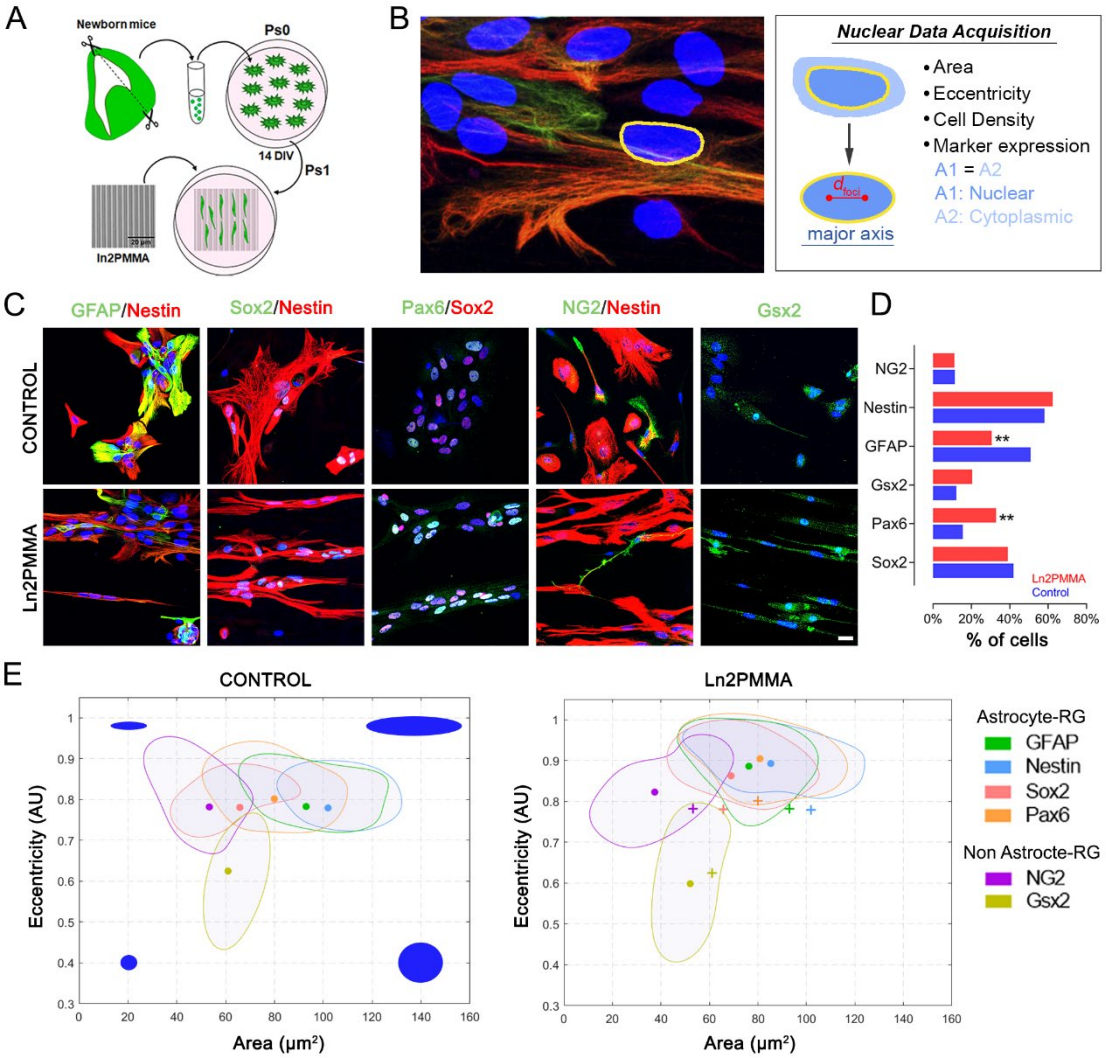

Figure 1: Glial cultures cell composition and nuclear morphology in control and ln2PMMA substrates. (A) Schematic diagram of cell culture protocol. **(B)** Schematics of nuclear data accuisition. **(C)** Representative pictures of primary cortical glial cells, grown in control and ln2PMMA substrates for 3DIV, labeled with different combinations of cell-specific markers for astrocytes (GFAP), immature astrocytes/RG (nestin), RG (Pax6), general stem cells (Sox2) and intermediate progenitors (NG2, Gsx2). Nuclei were stained with Hoechst (blue). Scale bar: 20μm. **(D)** Bar plot showing the percentage the different cell types in both control and ln2PMMA. **(E)** Density function probability plot with centroids representing the median values of eccentricity (y-axis) and area (x-axis) for each cell type. Blue shapes are used for reference of area-eccentricity combinations. Chi-square test **p<0.01.

To explore the effect of ln2PMMA on the nuclear area and eccentricity associated to each glial cell type we performed multivariate kernel density estimation. A nonparametric technique for population density estimation that assigns density probability regions for each cell marker, based on shared area and eccentricity (**Figure 1E**). We found no statistically significant differences between marker distributions; therefore we conducted t-tests to compare nuclear parameters individually between substrates within the same cell type (**Table S1**). This analysis showed that nuclei from nestin+, GFAP+, Pax6+ and Sox2+ cells were significantly deformed in ln2PMMA, adopting more elongated shapes, while nuclei from NG2+ and Gsx2+ cells did not significantly change their morphology. Together these data indicate that only cells form the direct astrocyte-RG lineage respond to ln2PMMA mechanical signals by changing their nuclear morphology.

Development of a logistic regression model to predict RG probability based on nuclear morphology parameters.

We evaluated whether nuclear deformation constitutes a hallmark in RG induction by constructing a logistic regression model. We defined prediction success as the ability to identify nuclei specific to RG, using nuclear area and eccentricity as predictors. The model relies on a binary response: RG or not RG, determined by the presence or absence of molecular markers indicative of the RG phenotype (Pax6+ or double Sox2+/nestin+). We used general linear models with the logit function to link the binary response to the linear predictor and estimates the probability of an event. In our case, the event was identifying whether RG cells exhibited a specific nuclear morphology, using glial cultures grown in control and ln2PMMA substrates for 3DIV. Importantly, cell-cell interactions are essential determinants of cell shape, proliferation, differentiation, and growth, and can revert the effect of the mechanical signals from the substrate [15]. Moreover, interactions among groups of precursor cells facilitate their coordinated differentiation during development, the so-called community effect [28]. Therefore, we included cell density in addition to nuclear area and eccentricity as predictors to account for this community effect. We developed multiple models of increasing complexity, by adding, suppressing, or conditioning these variables based on substrate type. The best model was selected following the Akaike Information Criterion (AIC), aiming to select the model that best explains the data with the fewest parameters. We refined the selected model using a step-by-step procedure to eliminate complex and non-significant terms. For example, by including cell density as an independent variable only in interactions, we reduced the AIC from 1313.062 to 1302.395 (**Table S2**). Most non-significant terms

were eliminated; however, terms relevant only in specific substrate interactions were retained, even if they were non-significant in the counterpart substrate. This refinement further reduced the AIC to 1300.325. Despite this improvement, it came at the cost of a reduction in AUC (Area Under the Curve), which measures the model's ability to distinguish between classes across all decision thresholds. This trade-off highlights the balance between reducing model complexity and maintaining predictive accuracy. We obtained a general model AUC of 0.73, with substrate-specific AUCs of 0.77 for ln2PMMA and 0.67 for the control substrate (**Table 1, Figure 2A**).

Table 1. Summary of model performance and significant terms. Top rows show AIC value for the general model and AUC values divided by substrate, including lower and upper confidence intervals (CI). Bottom rows show estimate values, standard error, z value and p-value for the selected terms of the model grouped by its substrate dependence. The full table is shown in the methods section.

Model	**AIC**	**AUC**	**Lower CI**	**Upper CI**
General	1300.325	0.73	0.7	0.76
Control		0.67	0.62	0.71
Ln2		0.77	0.73	0.81
Selected terms	**Estimate**	**Std. Error**	**z value**	**p-value**
Dependent on substrates				
Ln2PMMA	-9,45E+02	5,66E+02	-1.669	0.095
Control * E^3	-2,31E+02	8,84E+02	-0.261	0.794
Ln2PMMA * E^3	2,57E+03	7,32E+02	3.509	0.000
Ln2PMMA * A	-7,33E+00	4,74E+00	-1.546	0.122
Independent on substrates				
E^2 * D	5,15E+00	2,49E+00	2.068	0.039
A * D	-1,46E-01	4,13E-02	-3.522	0.000

For the different terms in the selected model, the sign of the estimated value indicates the direction of the prediction: positive values increase the probability of a specific RG nuclear morphology, while negative values decrease it. The z-value represents the relative weight or importance of each term in the model. Larger absolute z-values indicate a stronger impact of the corresponding term on the prediction. Finally, the relevance of each term is primarily determined by its p-value, which measures the statistical significance. A smaller p-value (e.g., < 0.05) suggests that the term is likely to have a meaningful contribution to the model, whereas larger p-values indicate weaker or negligible effects. The term associated with the ln2PMMA substrate alone did not meet the 5% significance level. However, in interaction with eccentricity, it demonstrated a substantial positive impact on the response (p-value < 0.01). As eccentricity increased, the probability of a nucleus being specific to RG cells became more defined. Therefore, in our modeling approach, we retained the effect of the ln2PMMA substrate on its own, as the term emerged during model construction and interacted with other variables. Similarly, we included the interaction between the control substrate and eccentricity,

despite it not being statistically significant and showing a negative effect on the response (z-value=-2.61E-01). Nevertheless, the inclusion of cubic eccentricity in interaction with both substrates underscored the relevance of increased eccentricity induced by the ln2PMMA substrate in favoring a distinct nuclear morphology specific to RG cells. Cell density was included in the model solely as an interacting variable. This approach reflects the impact of increased cell-cell interactions at higher cell densities, which can independently influence cell and nuclear morphologies regardless of the substrate. In our model, cell density demonstrated statistically significant interactions with area (p-value < 0.01) and eccentricity (p-value < 0.05), specifically in quadratic or cubic terms.

The presence of substrate-dependent terms allowed splitting the model in two equations, one for control substrate (**eq. 1**) and another for ln2MMA substrate (**eq. 2**).

(1) $\mathrm{logit}(\ \mathrm{P}\big(\mathrm{y}=1\big|(\mathrm{X},\mathrm{Control})\big) = \beta_0 + \beta_A\mathrm{A} + \beta_{\mathrm{A}^2}\mathrm{A}^2 + \beta_{\mathrm{A}^3}\mathrm{A}^3 + \beta_{E^3{}_C}\mathrm{E}^3 + \beta_{E^2{}_{*D}}\mathrm{E}^2 * \mathrm{D} + \beta_{E*D^2}\mathrm{E} * \mathrm{D}^2 + \beta_{A*D}\mathrm{A} * \mathrm{D} + \beta_{A*D^2}\mathrm{A} * \mathrm{D}^2 + \beta_{A^2{}_{*D}}\mathrm{A}^2 * \mathrm{D} + \beta_{A^2{}_{*D^2}}\mathrm{A}^2 * \mathrm{D}^2$

(2) $\mathrm{logit}(\ \mathrm{P}\big(\mathrm{y}=1\big|(\mathrm{X},\mathrm{Ln2PMMA})\big) = \beta_0 + \beta_{0Ln2} + \beta_A\mathrm{A} + \beta_{\mathrm{A}^2}\mathrm{A}^2 + \beta_{\mathrm{A}^3}\mathrm{A}^3 + \beta_{E^3{}_{Ln2}}\mathrm{E}^3 + \beta_{ALn2}A + \beta_{E^2{}_{*D}}\mathrm{E}^2 * \mathrm{D} + \beta_{E*D^2}\mathrm{E} * \mathrm{D}^2 + \beta_{A*D}\mathrm{A} * \mathrm{D} + \beta_{A*D^2}\mathrm{A} * \mathrm{D}^2 + \beta_{A^2{}_{*D}}\mathrm{A}^2 * \mathrm{D} + \beta_{A^2{}_{*D^2}}\mathrm{A}^2 * \mathrm{D}^2$

The expression *logit (…)* represents the application of the linear predictor to estimate the probability of the response y=1 (success, defined as being RG), using the variables X = area, eccentricity and cell density on control or ln2PMMA substrates. In the model, *β* corresponds to estimated coefficients*, A* to area, *E* to eccentricity, and *D to* cell density. Specific terms depending on substrate are indicated as C for control and Ln2 for ln2PMMA.

Statistical analysis was able to identify a RG-specific nuclear morphology

The analysis of surface plots showing area, eccentricity, and adjusted probability curves at different cell densities, revealed a "*RG nuclear region*" in which RG probability raises for medium sized and highly elongated nuclei, and is dynamically modulated by cell density (**Figure 2B**). However, the two equations, corresponding to control and ln2PMMA substrates (eq.1 and eq.2 respectively), resulted in different probability thresholds for the same nuclear morphology. This means that a nucleus with identical area and eccentricity values could be predicted as RG in one substrate condition but not in the other, raising the question of whether an RG-specific nuclear morphology truly exists. Thus, we evaluated the matching between control and ln2PMMA model equations predictions

(stablishing the probability identification threshold of RG at 0.5), and the percentage of experimentally observed RG (Pax6+ cells) in the same control and ln2PMMA datasets used for model construction. The control equation predicted 2% of RG in control and 11% in ln2PMMA, values far below the experimental observations of 15.5% of pax6+ cells in control, and 32.9% in ln2PMMA (**Figure 2C**). In contrast, ln2PMMA equation predicted 10% of RG in control and 33% in ln2PMMA much closer to the experimentally observed values of Pax6+ cells in both substrates (15% and 33% respectively, **Figure 2D**). Hence, the model used from that time on was exclusively based on ln2PMMA equation and named Radial Glia Mimetic (RGM) model.

When applying this model to different glial subtypes classified by marker expression of the data used for training the model, we observed a rightward shift of the RG probability curves for specific marker combinations. The highest shifts were observed for Pax6+/GFAP+ cells, followed by Pax6+/Nestin+, Pax6+, Pax6+/Sox2+, and finally Nestin+/Sox2+. This shift indicates that Pax6+ and double markers like Nestin+/Sox2+ are strong predictors of RG identity, with Pax6+/GFAP+ showing the greatest RG likelihood (**Figure S1 A-E**).

Moreover, despite their use as lineage markers, the expression of nestin or GFAP was not informative about the astrocyte-RG differentiation state, as RG predictions were quite similar (estimated probability p in 0.49-0.43; nestin+/GFAP+ > nestin+ > GFAP+) (**Figure S1 F-G, I**). However, our data indicate that the presence of those intermediate filaments are required for the capacity to move along astrocytic-RG lineage in response to mechanical stimuli, as in their absence cells have only residual probability to be RG ($p \leq 0.08$) (**Figure S1 N-P**).

The validity of the model was tested in several independent and previously unseen glial and neuronal cultures datasets at 3DIV, the timepoint used for constructing the model. We confirmed the accuracy of RG detection in glial cultures (ln2PMMA 21% of nuclei with $p>0.5$ and 22.7% Pax6+ cells; Control 6% of nuclei with $p>0.5$ and 11.2% Pax6+ cells, **Figure 2 G-H**), and the almost null RG probability observed in cultured neurons (2% $p \leq 0.02$, **Figure S2A**). Moreover, the proportion of active cycling cells in glial cultures, identified by the general proliferation marker Ki67 or the M phase-specific marker phosphohistone H3 (PH3), range from 6.1% to 17.6% at 3DIV and fit in a peak in the 0.1-0.2 RG probability consistently found in the density plots that account for around 10-20% of cells (**Figure S2B**). Therefore, nuclear changes during cell cycle progression in RG may have confounding effects of the RGM model predictions that need to be considered.

The LogOdds ratio function F(0) identifies RG-intrinsic nuclear mechanical constrains.

The accuracy of the RGM model in identifying RG cells based on nuclear morphology, regardless of the culture substrate, suggests the presence of cell-intrinsic mechanical factors that constrain the range of possible nuclear shapes in functional RG progenitors. If this holds true, the specific terms of the ln2PMMA model equation may capture these intrinsic nuclear constraints, which are likely enhanced by the RG-mimetic properties of the ln2PMMA substrate. To identify those nuclear constraints, we calculated the odds ratio function, a standard measure for assessing relative changes between probabilities, and here is applied to measure changes in ln2PMMA over control equations. The odds ratio function was defined as follows:

(3) $$Odds\ ratio = \frac{Odds\ (Ln2PMMA)}{Odds\ (Control)} = \frac{\mathrm{logit}(\ \mathrm{P}\left(\mathrm{y} = 1 \middle| (\mathrm{X}, Ln2PMMA)\right)}{\mathrm{logit}(\ \mathrm{P}\left(\mathrm{y} = 1 \middle| (\mathrm{X}, \mathrm{Control})\right)} = \exp(\beta_{0Ln2} + \beta_{E^3Ln2}\mathrm{E}^3 + \beta_{ALn2}A - \beta_{E^3C}\mathrm{E}^3)$$

Since all common terms between the equations cancel out, the odds ratio (**eq. 3**) depends only on nuclear area and eccentricity, both of which are cell-intrinsic parameters. By applying the logarithm to the odds ratio (**eq. 4**), we obtain a bidimensional function that defines the effect of ln2PMMA as mimetic of the embryonic RG niche, ensured compatibility with coefficients defined in linear regression models.

(4) $$Log(Odds\ ratio) = LogOdds\ ratio(A, E) = \beta_{0Ln2} + \beta_{E^3Ln2}\mathrm{E}^3 + \beta_{ALn2}A - \beta_{E^3C}\mathrm{E}^3$$

To analyze the behavior of the LogOdds ratio function, we created a surface plot at various levels of the function (**Figure 2E**). We defined the isolines of the LogOdds ratio function as lines in the plane defined by nuclear area and eccentricity that correspond to the same function value. When LogOdds ratio = 0, the resulting line, F(0), delineated the boundary at which the RGM model consistently elevated the probability of a nucleus being classified as RG, regardless of the substrate type (control or ln2PMMA). This F(0) line likely reflects an intrinsic mechanical constraint within the cells, establishing a theoretical threshold for RG nuclear morphology. Using this threshold, we identified the nuclear morphologies permissible within the RG region, which align with a particular observed nuclear area range of Pax6+ RG in our cultures (min = 34.75 μm², max = 139 μm², **Figure 2F**). It is worth noting that due to the removal of relevant parameters in the LogOdds ratio function with respect to the RGM model, all nuclei with >0.5 RG probability

were above the F(0) threshold, but not all nuclei above F(0) were identified as RG by the RGM model.

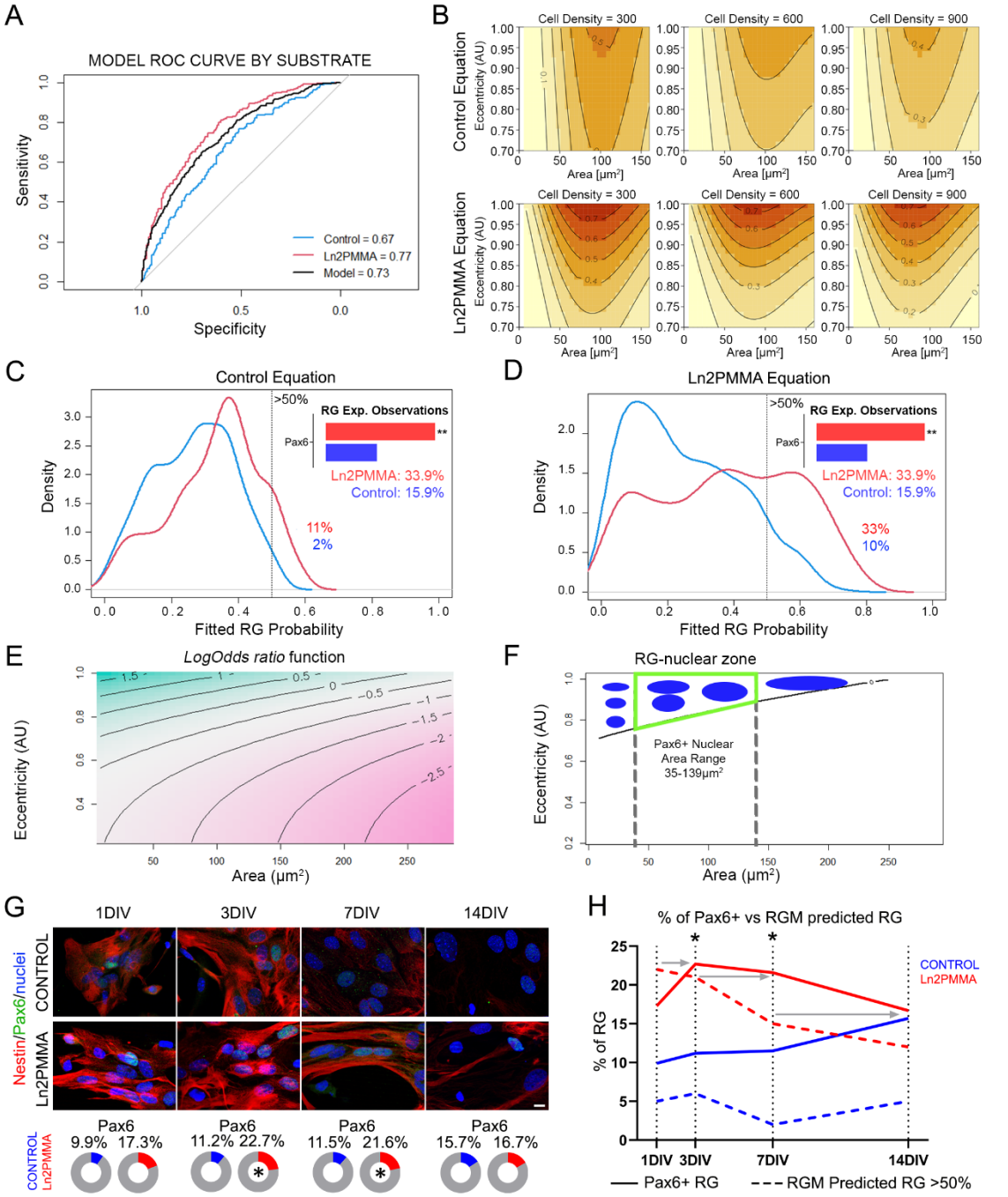

Figure 2: Model fitting, interpretation and identification of an RG-specific nuclear zone.
(A) ROC curves of the model: the general model ROC curve is shown in black, control equation in blue and ln2PMMA equation in red. Values in the legend show the AUC. **(B)** Surface plots of eccentricity (x-axis) and area (y-axis) of both model equations. Line curves represented the adjusted RG-probability at three different cell densities, 300, 600 and 900 cells/mm^2 in control and ln2PMMA. Density distribution of RG probabilities applying of control **(C)** and ln2PMMA **(D)** equations to the training data. Dashed lines delimitate the 0.5 threshold that stablishes RG identification. The numbers correspond to the percentage of cells with fitted probability over thershold of each case. Bars plot shows the proportion of cells expressing the PAX6 RG marker in the dataset. **(E)** Surface plot in function of area (x-axis) and eccentricity (y-axis) representing different levels of the LogOdds ratio function. **(F)** F(0) level of LogOdds ratio function (ascending black line) and representative RG nuclear morphologies. Vertical dashed lines delimitate the nuclear area range of Pax6+ cells. The theoretical RG nuclear area is highlighted in green. **(G)** Validation results. Representative pictures of primary cortical glial cells cells grown on control and ln2PMMA for 1, 3, 7 and 14 DIV, labeled with RG lineage markers nestin (red) and Pax6 (green), and nuclei stained with Hoechst (blue). Pie charts showing the proportion of Pax6+ cells at each time point. **(H)** Plot comparing % of RG calculated in base to Pax6+ cells (filled lines) or by the RGM model (dashed lines) at each time point. Gray arrows highlight the temporal shif of the RGM model predictions. Chi-square test, *p<0.05.

Nuclear deformation precedes gene expression changes in biomechanically induced astrocyte-RG transition

Mechanotransduction signals are rapidly transmitted from seeding, and glial cells adapt to the mechanical signals from the substrate and the neighboring cells, increasing astrocyte differentiation with time in culture. With the knowledge that RGM model accurately identify RG at 3DIV, we investigated the dynamics of nuclear deformation in control and ln2PMMA substrates from 1DIV to 14 DIV, wich encompass a complete cicle of astrocyte-RG-astrocyte transitions. In our culture conditions, the proportion of Pax6+ cells in control substrate was relatively high, considering that no functional RG is present in standard glial cultures, and showed no significant differences over time in (9.9-15.7%). As expected, RGM RG prediction in control substrate was stable over time, while significantly lower (5-10%) than the proportion of Pax6+ cells. In contrast, the proportion of Pax6+ RG in ln2PMMA varied with culture maturation, peaking significantly at 3 and 7DIV (22.7-21.6%), and resembling control substrate levels at the initial (1 DIV, 17.3%) and final (14 DIV, 16.7%) time points (**Figure 2G**). Accordingly, RGM RG predictions in ln2PMMA substrate were higher but shifted to earlier time points, peaking at 1-3 DIV (22–21%) and steadily decreasing at 7 and 14 DIV (15–12%), while still remaining higher than those predicted in the corresponding control substrate (**Figure 2H**). Given that we used Pax6 expression at 3DIV as a RG marker to construct the RGM model, this temporal shift between the amount of RG identified by the two methods was puzzling. One possible explanation is that nuclear deformation could preceed Pax6 expression changes during astrocyte-to-RG transitions. If that was the case, the RGM model would be predictive of fate direction, detecting RG and those cells commited to be RG, while ignoring cells at the initial stages of differentiation but before the Pax6 expression decay.

Ln2PMMA mechanical signal reduces lamins A-C/B1 ratio and increases nuclear β catenin in glial cells but not specifically in RG

Given that nuclear deformation preceeds Pax6 expression, we asked whether lamin proteins, the principal components of the nuclear lamina, will be involved in the early nuclear mechanotransductive response. The differential expression of lamin isoforms change during developmental progression and is associated with cellular mechanical adaptations to the microenvironment [29] [30]. To evaluate whether the relative expression of lamin genes in mouse RG-astrocyte lineage cells change during cerebral cortex development, we performed a metanalysis of publicly available transcriptomics datasets [31]. We found an inverse correlation between Lmna (codifying for lamin A and C proteins)

and Lmnb1 (codifying for lamin B1 protein) expression from E16 onwards (**Figure 3A**), leading to a sustained increase in Lmna/Lmnb1 ratio during late embryonic and early postnatal brain development, coincidental with astrocyte maturation. Therefore, we analyzed whether changes in lamins A-C/B1 ratio were involved in nuclear deformation observed during biomechanical driven astrocyte-RG transitions. For that, we immunostained glial cultures with lamins A-C and lamins B1 antibodies and analyzed the nuclear lamins A-C/B1 ratio at 1DIV, 3DIV and 7DIV (**Figure 3B**). At all times analyzed, nuclear lamins A-C/B1 ratio was significantly lower in In2PMMA compared to the control substrate. However, the ratio increased over time at similar rates in both substrates (**Figure 3C**). These data suggest that the nuclear lamina rapidly adapts its composition to In2PMMA mechanical signals and sustains these changes throughout the culture period. Then, we applied the RGM model to explore whether specific lamins A-C/B1 ratios were associated with nuclear deformation and increased RG probability. We observed a mild inverse correlation between the lamin A-C/B1 ratio and RG probability; however, no specific lamin A-C/B1 ratio was associated with increased RG probability (**Figure 3D-F**).

Mechanical regulation of gene expression involves changes in the activity and subcellular localization of transcriptional coregulators, such as β-catenin, yes-associated protein (YAP) and the transcriptional coactivator with PDZ-binding motif (TAZ) [32,33 34], proteins that are directly involved in RG organization and expansion [35 36 37 38]. Therefore, we wondered whether In2PMMA biomechanical induction of RG affect β-catenin and YAP/TAZ expression or subcellular distribution. To address this, we immunostained glial cultures grown on control and In2PMMA at 1DIV, 3DIV and 7DIV for β-catenin and YAP/TAZ detection, calculating the nuclear/cytoplasmic intensity ratio (Nuc/Cyto ratio) from confocal images (**Figure 3G, H, M**) and performing a linear regression analysis to evaluate dynamic nuclear-cytoplasmic shuttling over time. We found that β-catenin subcellular distribution in glial cells was similar in both substrates at 1DIV, but shuttling out of the nucleus along culture time significantly faster in control (higher negative slope) than in In2PMMA, which retained nuclear β-catenin along time (**Figure 3I**). Conversely, we found no significant differences in YAP/TAZ subcellular distribution in glial cells between substrates and over time (**Figure 3N**).

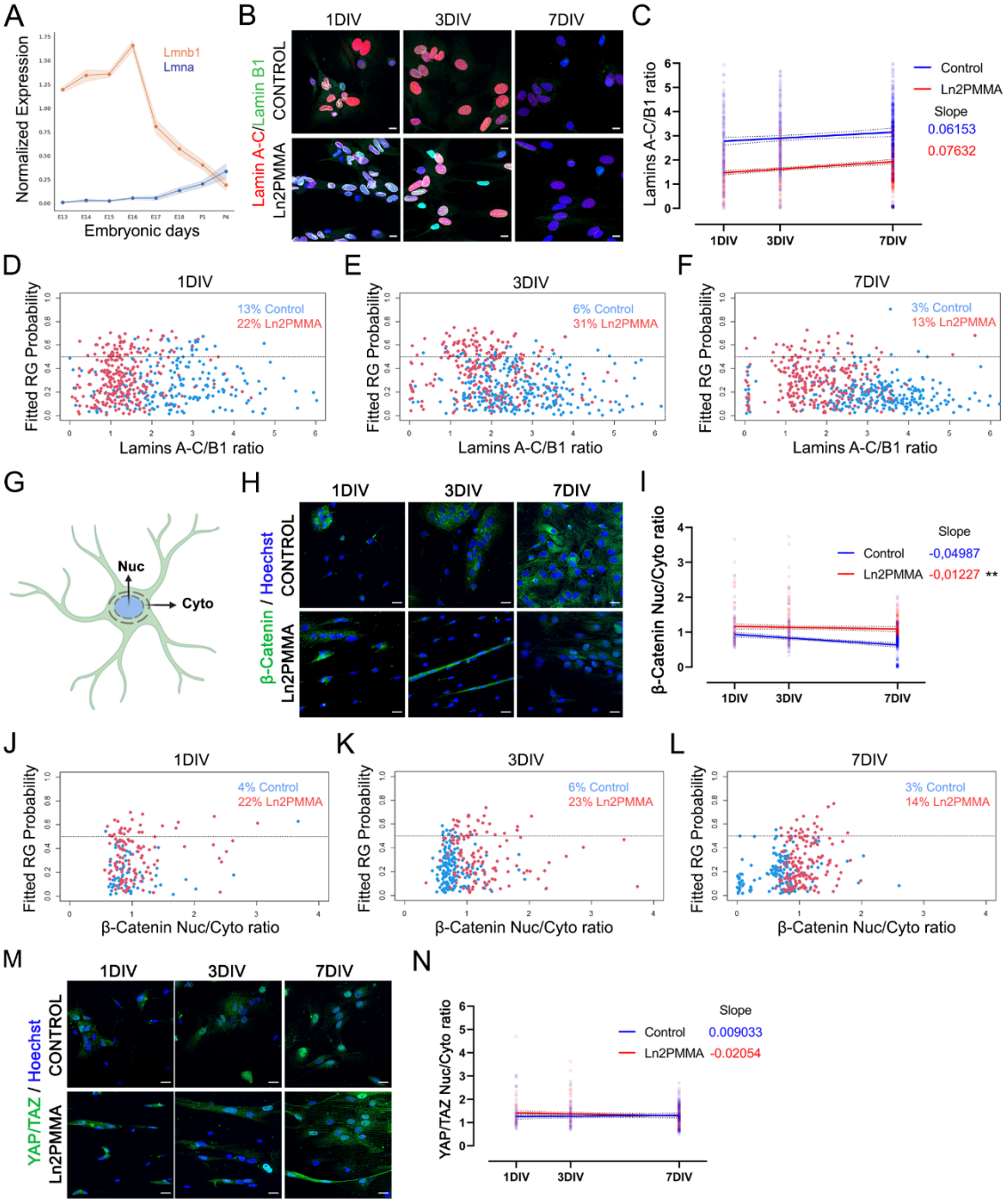

Figure 3: Ln2PMMA effect on lamins, β-catenin and YAP/TAZ expression and subcellular distribution across time in culture. (**A**) Plot showing a negative correlation between Lmnb1 and Lmna gene expression in RG-astrocyte lineage cells during brain development, normalized by the average of Lmna gene expression at E13 (data from Di Bella et al., 2021). (**B**) Confocal images of glial cells grown for 1-7 DIV on control and ln2PMMA substrates, and immunostained for lamins A-C (red) and B1 (green). Hoechst 33342 (blue) stained nuclei. (**C**) Linear regression analysis of lamins A-C/B1 ratio in control and ln2PMMA across time in culture. Scatter plots of fitted RG probability for increasing lamins A-C/B1 ratios at (**D**) 1DIV, (**E**) 3DIV and (**F**) 7DIV. Dashed line delimits 0.5 probability. Control substrate in blue and Ln2PMMA in red, the numbers correspond to the percentage of cells with fitted probability to be RG > 0.5. (**G**) Schematic of the nuclear area and equal cytoplasmic perinuclear area segmentation used for Nuc/Cyto ratio calculation (see methods). (**H**) Confocal images of glial cells cultured for 1-7DIV on control and ln2PMMA, immunostained for β-catenin (green) and counterstained with Hoechst (blue) to identify nuclei. (**I**) Linear regression of β-catenin Nuc/Cyto ratio over time. Scatter plots of fitted probabilities for increasing β-catenin Nuc/Cyto ratios at (**J**) 1DIV, (**K**) 3DIV and (**L**) 7DIV. Dashed line delimits 0.5 probability. Control substrate in blue and Ln2PMMA substrate in red, numbers correspond to the percentage of nuclei with > 0.5 probability to be RG. (**M**) Confocal images of glial cells grown for 1-7DIV on control and ln2PMMA substrates immunostained for YAP/TAZ (green) and counterstained with Hoechst (blue) to identify nuclei. (**N**) Linear regression analysis of lamins A-C/B1 ratio in control and ln2PMMA across time in culture. 487-553 cells from different biological samples were used for each time and condition. Scale bar: 20µm. Statistical analysis for linear regression ANOVA **p<0.01.

RG nuclear morphology is linked with specific nuclear calcium dynamics.

Spontaneous intracellular Ca^{2+} waves are major components of RG and astrocytic signaling, and are essential in regulating proliferation, structural scaffold maintenance, gene transcription and differentiation [39] [40] [41]. Therefore, we performed fluorometric calcium imaging using the Ca^{2+} indicator Oregon Green™ 488 BAPTA-1, AM (OGB), which binds free intracellular calcium in living cells, to directly assess whether RG glia identified by their nuclear morphology by our RGM model have specific intracellular Ca^{2+} dynamics. After Ca^{2+} imaging, the recorded slices were fixed and immunostained for Pax6 and nestin detection, to correlate individual cells activity with RG marker expression (**Figure 4A-B**). To determine relative differences in nuclear intracellular Ca^{2+} dynamics between cells grown in control and ln2PMMA substrates, we defined regions of interest (ROI) corresponding to the cell nuclei. We used these ROIs to mask the image, normalized the signal by subtracting the sample background to ensure comparable reference levels across samples, and quantified the signal magnitude over time (**Figure 4C**). We found that Ca^{2+} fluorescent signal was significantly lower in glial cell nuclei in ln2PMMA compared to control substrate, both in absence and presence of 2mM extracellular Ca^{2+} (**Figure 4D**). Then, we analyzed the presence of spontaneous Ca^{2+} oscillations (transients) by calculating the average of $\Delta F/Fo$ (basal/resting value) at baseline (calcium-free extracellular medium) and calcium (2mM extracellular calcium) conditions. Consistent with their lower intracellular Ca^{2+}, glial cells grown on ln2PMMA had significantly less and smaller spontaneous nuclear Ca^{2+} transients, both, in absence and presence of extracellular Ca^{2+} (**Figure 4E**). When segregated by cell type, Pax6+ RG had higher nuclear intracellular Ca^{2+} and larger calcium transients than non-RG cells in both substrates, despite a mild reduction in ln2PMMA (**Figure 4F, H**). By applying our RGM model, we found that RG cells had significantly higher nuclear intracellular Ca^{2+} levels and spontaneous Ca^{2+} transients than non-RG cells, regardless of the substrate type and the presence or absence of extracellular Ca^{2+} (**Figure 4G, I**). These data specifically link the RG nuclear morphology identified by our RGM model to specific intracellular calcium dynamics, a key physiological feature of RG.

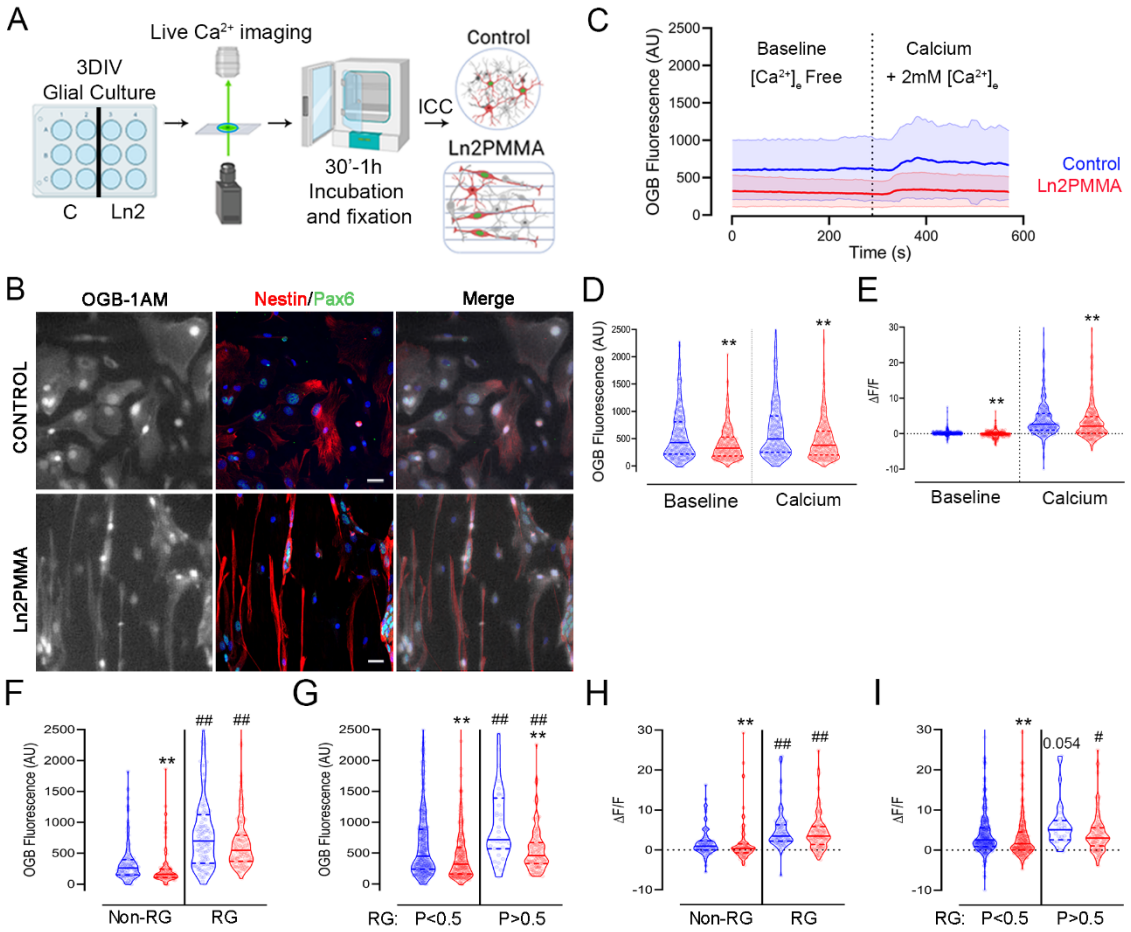

Figure 4: Evaluation of intracellular Ca^{2+} concentration in glial cells grown on control and ln2PMMA substrates. (A) Experimental design. **(B)** microscopy images of glial cells grown for 3-4 DIV on control and ln2PMMA substrates live-loaded with OGB (white) and immunostained after fixation for RG markers Pax6 (green) and nestin (red), using Hoechst 33342 for nuclei (blue) detection. **(C)** Intracellular Ca^{+2} levels were analyzed by background subtraction (F(t)-background) method and represented as signal mean +/- 95% CI (shadow area) in control (blue) and ln2PMMA (red) substrates. Baseline are extracellular Ca^{+2} free and calcium has 2 mM $CaCl_2$. Violin plots representing **(D)** average fluorescence intensity in each nucleus and **(E)** spontaneous nuclear Ca^{2+} transients (average ΔF/Fo), at baseline and calcium conditions in glial cells grown on control and ln2PMMA. Violin plots representing the average fluorescence intensity in each nucleus of **(F)** Pax6+ RG and non-RG cells, **(G)** RGM model predicted RG (p>0.5) and non-RG p<0.5 in calcium condition. Violin plots representing spontaneous nuclear Ca^{2+} transients in **(H)** Pax6+ RG and non-RG cells, and **(I)** RGM model predicted RG (p>0.5) and non-RG p<0.5, in calcium condition. Scale bar: 25µm. Statistical analysis: Kruskal Wallis and multiple comparison post-hoc tests. Differences between control and ln2PMMA * p<0.05, **p<0.01; differences cell types # p<0.05, ## p<0.01. Four different samples and more than 63 cells for each condition.

Conservation of RG nuclear morphology constraints across species

We constructed our RGM model using nuclear data from 2D images of glial in vitro cultures at different cell densities, intentionally excluding highly confluent zones where the lack of space and cell-contact inhibition drives glial cells out of the cell cycle and promotes astroglia differentiation. This design choice limits the applicability of the RGM model in such conditions, where it could still be applied but previning extrapolation. On the other hand, the LogOdds ratio function is only based on nuclear morphology parameters and is not limited by cell density restrictions. Therefore, it can be applied to highly confluent cell cultures or even brain tissue sections. To showcase its capabilities,

we used the LogOdds ratio function at F(0) threshold, restricted to the nuclear area range of Pax6+ cells, as an initial approach to inquire inter-species conservation of RG cells nuclear morphology *in vivo* and *in vitro*.

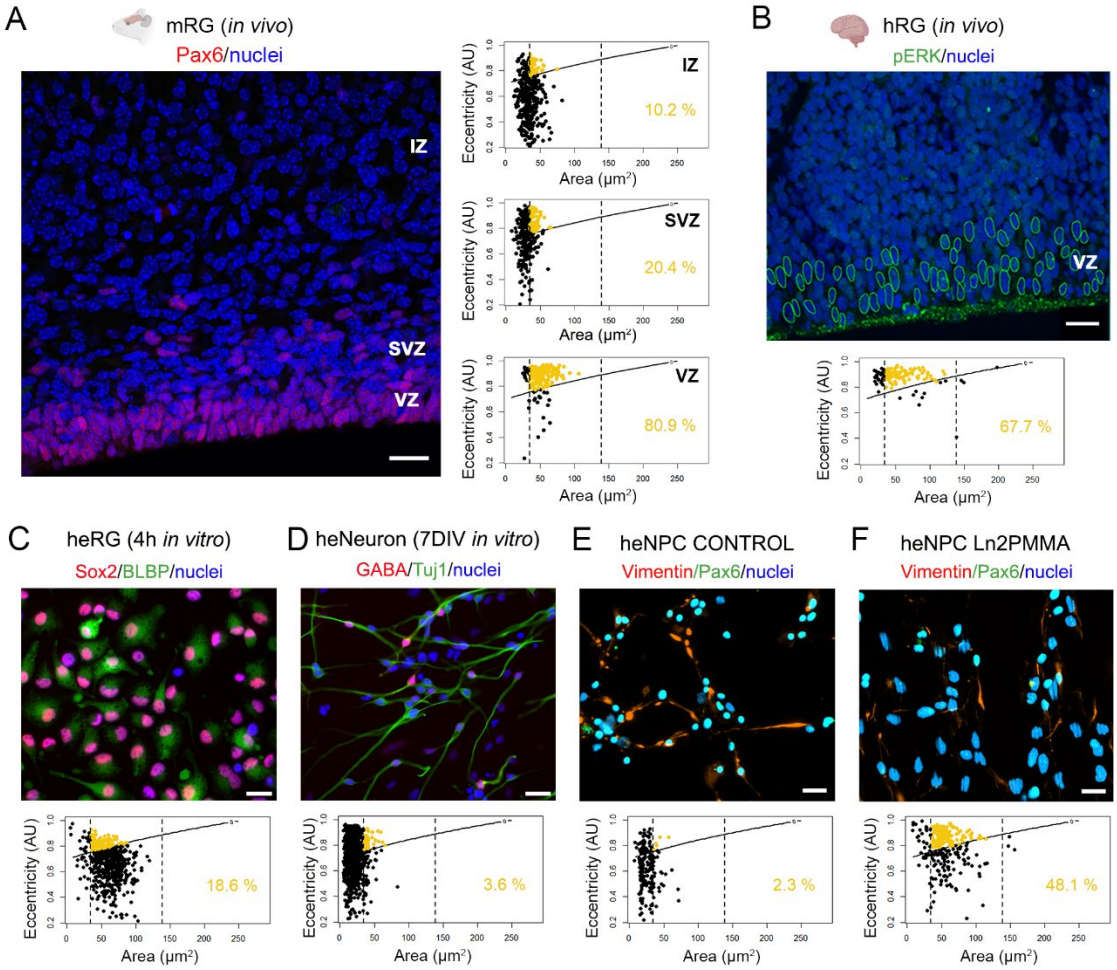

Figure 5: Conservation of RG nuclear morphology between mice and human. Microscopy images and corresponding surface plots representing the log-odds ratio function at F(0). Yellow dots and percentages correspond to the nuclei fitting into the RG nuclear area stablished by our RGM model. **(A)** Coronal section of the mouse cerebral cortex at embryonic day 18 (E18) immunostained for Pax6 and Hoechst 33342 for nuclei (blue) detection. **(B)** Coronal section of fetal human cerebral cortex at gestational week 10 (GW10) immunostained with pERK and using DAPI to label nuclei (blue). **(C)** hRG culture obtained from the embryonic brain shown in **(B)** and cultured for 4h in a flat control substrate immunostained for SOX2 (red) and BLBP (green), and using DAPI to label nuclei (blue). **(D)** 7DIV hneurons differentiated form hRG in **(C)** immunostained for GABA (red) and Tuj1 (green), and using DAPI to label nuclei (blue). HeNPC grown on control substrate (Matrigel coated) **(E)** and Ln2PMMA **(F)**, immunostained for Vimentin (red) and Pax6 (green) using Hoechst 33342 for nuclei (blue) detection. In each panel, the surface plots in function of area (x-axis) and eccentricity (y-axis) represent the LogOdds ratio function at F(0), with vertical dashed lines delimitating the nuclear area range of Pax6+ cells in mouse glial cultures (Amin=34.75µm2 / Amax=139µm2). Scale bar: 20µm. VZ: ventricular zone; SVZ: subventricular zone; IZ, intermediate zone.

Using cortical sections of embryonic day 18 (E18) mice, we analyzed the nuclear morphology of cells located in the ventricular zone (VZ), mostly Pax6+ RG, cells located in the subventricular zone (SVZ), mostly intermediate progenitors, and cells in the intermediate zone (IZ), at this age mainly occuped by migrating neurons. Consequent with this cellular distribution, we found that the percentage of nuclei withing the RG region

were 80.9% in the VZ, 20.4% in the SVZ, and 10.2% in the IZ (**Figure 5A**), closely resembling our *in vitro* data and supporting the notion that RG nuclear constraints are present in vivo.

To inquire whether similar nuclear constraints were present across species, we analyzed neocortical histological sections and *in vitro* RG cultures derived from 10-15 gestional week human fetuses (material derived from[42,43]). In the human embryonic cortical sections, human RG (hRG) nuclei were identified by its location in the VZ and pERK expression, as ERK signaling is required for RG maintenance and cortical lamination [44]. Consistently with our findings in mouse, 67.7% of putative hRG nuclei in the VZ fitted into the model defined RG nuclear area (**Figure 5B**), supporting the evolutive conservation of the nuclear constraints identified with our RGM model.

To evaluate whether tissue dissociation-induced loose of basal and apical anchorage and further grown and differentiation in culture impact nuclear morphology, we analyzed primary cultures of hRG obtained from cortical dissections of midgestation fetal brains. Immunomagnetic cell sorting allowed purification of hRG which were cultured and imaged at 4h and after 7DIV, to track their differentiation into neurons [42,43,45]. Culture hRG for 4h in vitro in standard poly-D-lysine (PDL) coated flat substrate induced a rapid exit from the model defined RG region, passing from 67.7% to 18.6% of nuclei (**Figure 5C**). Moreover, after 7DIV only a residual 3.6% nuclei fitted within the RG region, indicating that hRG-derived neurons have a clearly different nuclear morphology (**Figure 5D**). We next tested if In2PMMA substrate anisotropy favors the acquisition of potential RG nuclear morphologies in neural cells at early stages of differentiation. In these experimentes, we utilized human stem cells-derived NPCs (hNPCs; for more details see methods section). We found that only 2.3% of hNPC nuclei fell within the RG region when cultured in control PDL substrates (**Figure 5E**), while in In2PMMA, nearly 50% of hNPC nuclei fitted in the RG nuclear region (**Figure 5F**). Taking together these data indicated that the topology of the embryonic RG niche imposes RG nuclear morphology constraints that are conserved between mouse and human through evolution.

Discussion

The mechanoresponsive capacity of the nucleus relays on its capacity to deform in response to tension, altering their nuclear envelope composition, chromatin organization and gene expression [46,19]. We took advantage of a non biodegradable micro 3D substrate (In2PMMA) that mimicks the mechanical anisotropy and surface properties of the

embryonic RG niche, and induces astrocyte to funcional RG transformation *in vitro* [14], to investigate the relevance of nuclear morfology in cell fate adquisition. Here we have shown that mechanical signals are rapidly transmitted to the glial cell nucleus, which adapt their shape and size before significant changes in the expression of RG molecular markers. By the development of a multivariate logistic regression model that take into account the structural anisotropy of the embryonic RG niche, RGM model, we demonstrated that the mechanical signals from ln2PMMA force the glial cell nucleus to adopt a specific morphology, which was restricted to what we defined as the RG nuclear zone. This morphological change was associated with lower lamins A-C/B1 ratio and sustained nuclear β-catenin, which occurs before the expression of RG molecular markers. Moreover, RG nuclear morphology correlates with specific intracellular calcium dynamics, which are clearly distinguishable from those observed in non-RG cells. Finally, we have shown that RG nuclear constraints are conserved *in vivo/in vitro* as well as between mice and human.

One of the principal challenges in RG classification, and neural cell classification more broadly, is their inherent heterogeneity and the lack of specific markers, wich are often shared among different cell types, making accurate classification uncertain [47,48,49,50]. For instance, Sox2, while serving as a marker for RG, is also a general stem cell marker. Similarly, nestin is expressed not only in RG but also in immature and reactive astrocytes and mesenchymal SC. Pax6, another RG marker, is also expressed in the early eye neuroectoderm and in specific neuronal subsets. Conversely, the widely used astrocytic marker GFAP is also expressed in ependymal cells and NSC, further complicating the specificity of these markers. Therefore, the development of a multivariate logistic regression model to predict RG probability based on nuclear morphology parameters provides a novel classification tool to more precisely stratify cell types as well as cell states, and with the potential to predict cell behaviors [51,52].

Recent studies on the dynamics of mechanosensitive NSC differentiation have revealed that lineage commitment occurs within the 2-3 days after initial adhesion [53] coincidental with our observation that significant increases in the expression of Pax6 RG marker in glial cells occurs after 3DIV on ln2PMMA (**Figures 1, 2**). Thus, the constructed model was developed using data from 3DIV glial cultures, and assigns RG probabilities based on nuclear area and eccentricity, and a binary response determined by the presence or absence of established neural cell-type molecular markers (Pax6+ or double nestin+/Sox2+ for RG). We constructed the model iteratively using maximum likelihood estimation to assign probabilities associated with RG classification and following the standars described by the Committee on Credible Practived of Modeling and Simulation

on Healthcare described in [54]. By including cell density as a covariable, we also consider the “community effect”, a biologically relevant concept during cell differentiation and tissue patterning [55]. One strength of the model was the inclusion of non-linear interactions, such as quadratic and cubic variable coefficients, which retain biological interpretability. Additionally, its substrate-dependent nature underscores the critical relationships between topography, cell density, and nuclear morphology. However, the selected model yielded two separate equations for RG probability, one associated with control substrate and another for ln2PMMA substrate, each exhibiting different levels of accuracy (AUC 0.67 for control and 0.77 for ln2PMMA). This discrepancy raises some concerns, as a given nuclear shape was expected to yield the same substrate-independent RG probability. Nevertheless, during model verification, the predictions for RG probabilities > 0.5 from the ln2PMMA equation reproduced more accurately the experimentally observed percentages of Pax6+ RG, regardless of the substrate used, compared to the control equation. As ln2PMMA mimics the anisotropic architecture of the embryonic RG niche in the developing brain [14], we named the model based exclusively on the ln2PMMA equation as the Radial Glia Mimetic (RGM) model. The RGM model revealed a specific nuclear shape associated with RG functional phenotypes in cells expressing nestin/GFAP intermediate filaments, which are the ones with the capacity to move along astrocytic-RG lineage in response to the mechanical stimulus. Moreover, the model accurately identified cells that were unlikely to be RG, further refining its classification capability. Importantly, our RGM model was validated with real data of glial cultures at 3DIV, instead of using cross-correlation or simulated data, increasing its robustness and consistency [56].

As previously described, the timeline of mechanosensitive NSC differentiation [53] aligns with our observation that significant increases in Pax6 RG marker expression occur after 3DIV in ln2PMMA cultures. However, RG-specific nuclear shapes were significantly increased at 1DIV, and declined notably by 7DIV, days before significant changes in Pax6 expression. This temporal shift between nuclear shape and Pax6 expression suggests that nuclear deformation precedes mechanically-induced fate commitment and subsequent Pax6 expression. To investigate the molecular mechanisms underlying this early nuclear deformation, we analyzed the lamins composition of the nuclear lamina, a key regulator of nuclear mechanics and NSC fate [57,29]. Our metanalysis of lamin genes expression in mouse RG-astrocyte lineage across development (dataset from [31] revealed an inverse correlation between Lmna (codifying for lamin A and C proteins) and Lmnb1 (codifying for lamin B1 protein) expression from E16 onwards, leading to a sustained increase in Lmna/Lmnb1 ratio during late embryonic and early postnatal brain

development, coincidental with astrocyte maturation. Therefore, the reduced Lmna/Lmnb1 ratio observed in Ln2PMMA, more resemblant to the embryonic situation, might have a relevant role in the de-diferentaition process.

To further study the molecular mechanisms underlying mechanically driven RG induction, we analyzed the expression and subcellular localization of β-catenin and YAP/TAZ. These proteins function as mechanosensitive transcriptional co-factors [46] and are crucial NSC regulators, involved in the development and maintenance of RG architecture [3]. At the molecular level, the nuclear β-catenin/TCF complex binds Pax6 promoter, inducing Pax6 transcription. Conversely, conditional β-catenin ablation in RG reduces Pax6 expression and RG self-renewal, increasing the production of astrocytes [58]. Therefore, the sustained preferential nuclear localization of β-catenin observed in glial cells cultured on ln2PMMA could be one of the mechanically driven inducers of Pax6, forcing competent cells to adopt an RG fate, despite no specific β-catenin nuclear-to-cytoplasmic ratio being directly associated with an increased RG probability. On the contrary, the rapid β-catenin nuclear extrusion in flat control substrate might prevent Pax6 expression, promoting astrocyte differentiation. Although we found no significant changes in the protein expression and subcellular distribution of YAP/TAZ, their involvement cannot rule out, as direct protein interactions between YAP and β-catenin are proposed to play a role in transducing mechanical cues into NSC differentiation programs [53].

Finally, we previously demonstrated that ln2PMMA-induced RG suport neuronal migration [14]. A critical characteristic of RG is the generation of spontaneos calcium waves, wich regulate proliferation, neurogenesis and neuronal migration [39,40]. Therefore, the strong correlation between RG nuclear morphology and a precise spontaneous calcium dynamics reinforces the physiological link between nuclear morphology and function, as well as the reliability of our RGM model for identifying functional RG.

The accuracy of the RGM model in identifying RG cells based on nuclear morphology, irrespective of the culture substrate, suggests the existence of intrinsic mechanical factors within the cells that constrain the range of possible nuclear shapes in functional RG progenitors. As already described, the LogOdds ratio function defines the effect of ln2PMMA anisotropy as mimetic of the embryonic RG niche. Therefore, the F(0) boundary may represent an intrinsic mechanical factor within the cells, and by narrow down tothe Pax6+ nuclear area range, we established a theoretical threshold for the functional RG nuclear region based exclusively on nuclear morphology parameters (area and eccentricity) without assigning any specific RG probability. Consistent with our

hypothesis, segmented RG nuclei from mouse and human cortical sections images fell neatly within this delimited RG region, supporting the evolutionary conservation of RG nuclear constraints. Furthermore, nuclei from acute primary hRG cultures derived from comparable fetal brain regions, as well as from hNPC cultures grown on standard PDL coated flat substrates, mostly fell outside the RG region. On the contrary these flat culturing-induced effects were mitigated when hNPCs were grown on In2PMMA, with nuclei adopting RG nuclear morphologies similar to what occurs whith mice glial cultures, further validating the model's biological relevance. All together, these data suggest that the absence of mechanical signals from the microenvironment during culture on flat substrates disrupts RG structural anisotropy, affecting nuclear morphology, functionality and cell fate. Thus, it would be recommended the use of anisotropic RG-mimetic substrates, like In2PMMA, to improve the maintenance of hRG and hNPC stemness.

Conclusions

This study underscores the critical role of nuclear morphology and mechanosensitive signaling in RG fate acquisition and functional identification. Using the anisotropic In2PMMA substrate as a model system, we demonstrated that mechanical cues rapidly shape nuclear morphology, preceding the expression of RG-specific molecular markers. Our RGM model, developed from these observations, effectively predicts RG probability based on nuclear morphology parameters, providing a robust classification tool for identifying functional RG *in vitro*.

In summary, this work provides a framework for studying the interplay between nuclear mechanics, morphology, and cell fate decisions, offering a novel approach for RG identification and differentiation studies. Future research should focus on refining anisotropic culture systems, exploring the influence of mechanical signals on other neural cell lineages, and elucidating the molecular mechanisms driving nuclear deformation and RG fate commitment. Additionally, integrating computational tools to model and analyze the complex interactions between mechanical and molecular cues could provide deeper insights, with potential applications in regenerative medicine and developmental biology.

Author's contributions: Conceptualization: SA, JPS, JA, CB. Design of the work SA, JPS. Experiments: JPS (mouse related experiments), JAO (human related experiments). Image acquisition and processing: JPS. Calcium experiments: RS, JPS. Software development for image and calcium analysis: CB. Data processing: JPS. Data analysis: JPS, SA. Statistical model generation: JA, JPS. Single-cell transcriptomics metanalysis: LG. Human sample in vivo and in vitro experiments: AO. Supervision SA, JA, CB. Original draft preparation SA. JPS. Writing rewiew and editing all authors. All authors read and aprobed the final manuscript.

Funding: This work was supported by the grant PID2020-115748RB-I00 from Spanish Ministry of Science and Innovation (MICINN) to SA. PID2023-150234NB-I00, and Gobierno de Aragón under Research Group E46_23R: Modelos Estocásticos to JA. We are also grateful to funding sources PID2020-114407RA-I00 and CNS2023-144820 (JAO) funded by MICIU/AEI/10.13039/501100011033 and by European Union NextGenerationEU/PRTR. Researchers also thank Programme/Generalitat de Catalunya (2021 SGR 00344) (SA and JAO), the Ramon y Cajal fellowship RYC2019-026980-I (JAO), and Maria de Maeztu Units of Excellence: Institute of Neurosciences, University of Barcelona (JAO and SA).

Data availability statement: All study data are included in the article and/or supplementary data and in the https://github.com/PepPau/RGM-model-main-scripts.git. Original data will be available upon request when this article will be published.

Acknowledgements: We also thank the Biologia-Bellvitge Unit from Scientific and Technological Centers (CCiTUB), Universitat de Barcelona, and Benjamin Torrejón for their support and advice on confocal microscopy technique, and Marta Cuenca and Cristina Martinez for their technical support in preparing human NPC cultures on control and In2PMMA substrates.

Conflicts of interest: The authors declare no competing or finantial interest.

STAR Methods

Animals and cell cultures

The Ethical Committee for Animal Experimentation of the University of Barcelona and the Generalitat de Catalunya with order nº: 9656 approved animal housing and all experimental procedures in accordance with Spanish and EU regulations.

Cortical primary cultures

Cortical glial cells were obtained from newborn (P0-P1) Swiss albino mice of both sexes. Briefly, after brain extraction, cerebral cortices were dissected out free of meninges in dissection buffer (PBS + 0.6% of glucose (Sigma), 0.3% bovine serum albumin (BSA) (Sigma)) and digested with 5 ml of trypsin (Life Technologies) with 500µl of DNAse I (Sigma) for 10 minutes at 37º. The tissue was mechanically dissociated in growing medium (GM) Dulbecco's Modified Eagle Medium (DMEM, Biological Industries), 10% normal horse serum (NHS, GIBCO), 1% penicillin-streptomycin (P/S, Biological Industries) and 1% L-glutamine (Biological Industries). After centrifugation and resuspension, passage 0 (Ps0) cells were plated in flasks and grown for 14 days. To remove contaminating microglial and oligodendroglia progenitor cells, cultures were shaken overnight at 37ºC followed by a change of medium the day before starting the experiment (adapted from[59]). For all experiments, adherent Ps0 glial cells were dissociated with trypsin, counted, and plated on the different substrates (borosilicate glass coverslips or Ln2PMMA) at a density of 2-4x10^4 cells/cm^2 in 24 wells, and 2x10^6 cells in P60 culture plates, and grown for 1-14 DIV in Neurobasal™ (NB, Gibco), 3% NHS, 1% P/S and 1% L-glutamine (experimental medium, EM) (Ps1). When plated in 24 wells on borosilicate glass or ln2PMMA we first spread the drop with cells (60µl) very carefully onto their respective surfaces and left 20-30 minutes at 37ºC in the incubator to favor cell adhesion, note that surfaces were uncoated and are hydrophobic [59]. Then each well was filled with the remaining medium required (440µl).

Human induced pluripotent stem cells (iPSCs)

Human induced pluripotent stem cell (iPSCs) line 18a and embryonic stem cell (ESC) line HUES 64 (Harvard Stem Cell Institute) were cultured in mTeSR medium on Matrigel-coated plates (ThermoFisher BD354277). Cell lines were transferred to University of Barcelona-IDIBELL after Generalitat de Catalunya Health Department's approval and material transfer agreement (MTA) stablished between Institutions (Signed by Ortega JA as principal investigator). The cells were fed with fresh mTeSR medium daily (Stem Cell Technologies - 85850). For thawing or splitting, iPSCs were resuspended in DMEM/F-

12 media (FISHER SCIENTIFIC, Gibco, 11574546) and cultured in mTeSR supplemented with 10 µM ROCK inhibitor (RI) (Bio-Techne, ToCris, #1254) for 24-48 hours. Basic passaging was performed using EDTA (0.5 mM), while accutase (Innovative Cell Technologies - AT 104-500) was used for human neural progenitor cells (hNPCs).

Human neural progenitor cells (hNPCs)

Human neural progenitor cells (hNPCs) were derived from the human iPSC or ESC following the protocol previously described by (Topol et al., 2015). Briefly, iPSCs were dissociated with accutase (Sigma-Aldrich) and replated in matrigel-coated plates and mTESR media with RI, to obtained a 70% confluency by the following day (day 0), when mTESR was replaced by N2/B27 media [DMEM/F-12 with 1X N-2 (100X, 12013479, Gibco), 1X B27™ (50X, 11530536, Gibco), and 20ng/ml of recombinant human FGF-basic – (PHG0264, Fisher Scientific)] supplemented with dual SMAD inhibitors (0.1M LDN193189 and 10M SB431542) for 6 days. Media was changed on a daily-base, and from day 7, we also incorporated 1 µg/ml laminin (from day 7) to the media. By day 12 neural rosettes were dissociated utilizing STEMdiff™ Neural Rosette Selection Reagent (StemCell Technologies, #05832). The dissociated NPC were resuspended and replated in matrigel-coated plates with NPC media (DMEM/F-12 supplemented with N2 and B27).

Fetal tissue samples and human radial glia cell (RGC) cultures

Fetal tissue samples were obtained and utilized at Zecevic's laboratory (University of Connecticut Health Center). Samples were originally sourced from Advanced Bioscience Resources (ABR) and Human Developmental Biology Resource (HDBR), after parental written consent and approval from the Ethics Committees of the participating Institutions [42,43]. Human materials were handled with special care and following all necessary requirements and regulations set by the Ethics Committee of the University of Connecticut and the Helsinki Declaration. Samples were transferred to University of Barcelona-IDIBELL after UB-Bioethic Committee approval and MTA stablished between Institutions (Signed by Ortega JA as principal investigator). The fetal brains used in the study exhibited no signs of disease or abnormalities upon thorough neuropathological examinations. The developmental stage was determined based on gestational weeks after conception and ultrasound findings. The tissue was collected in oxygenated Hank's balanced salt solution (Invitrogen) and transported on ice. After dissection, cortical tissue was mechanically and enzymatically dissociated using 0.025% trypsin-EDTA (Invitrogen) and DNAse I (2 mg/mL, Sigma-Aldrich). The resulting cells were cultured in poly-D-lysine (Sigma-Aldrich) coated flasks containing proliferation medium (PM), consisting of DMEM/F12 (Invitrogen), B27 supplement (Invitrogen), basic fibroblast

growth factor (bFGF; 10 ng/mL, Peprotech), epidermal growth factor (EGF; 10 ng/mL, Millipore), and penicillin/streptomycin (Invitrogen). After cell expansion, we utilized MACS® Technology to immunomagnetically sort human RGCs from fetal brain derived cultures with anti-CD15-antibody-coated microbeads (Miltenyi Biotech). Detailed description of the protocol followed is described in [42,43]. Human RGCs were cultured on poly-D-lysine-coated and grown with PM for expansion for 1-3 days. For differentiation purposes, bFGF and EGF was removed from culture media.

For immunocytochemistry of human RGC cultures, cells were fixed with 4% paraformaldehyde for 30 minutes, blocked for 1 h in PBS with 0.1% normal goat serum (Gibco) and 0.1% Triton (Sigma-Aldrich), and incubated cells overnight at 4 °C with the primary antibodies Sox2 (Santa Cruz biotechnologies, sc-17320) and BLBP (Abcam, ab27171) for RGC identification; and GABA (Sigma, WH0026468M1) and TUJ1 (Dako, PRB-435P) for neuron identification. Next day, cells were incubated for 1h with the Alexa488- or Alexa555-conjugated secondary antibodies (1:500, Molecular Probes). Cell nuclei were counterstained with bisbenzimide (Hoechst 33342) (Sigma-Aldrich).

For immunohistochemistry, fetal forebrain blocks were fixed in 4% paraformaldehyde overnight, cryoprotected in PBS + 30% sucrose, and TissueTek OCT blocks were made by freezing in liquid nitrogen for subsequent sectioning 15-µm sections). Sections were blocked in Tris-NaCl-Tween buffer (TNT) [0.1 M, pH7.5 Tris-HCl (Thermo Fisher Scientific); 0.15 M NaCl (Thermo Fisher Scientific); and 0.05% Tween] with 0.5% blocking reagent (Roche) and incubated overnight at 4 °C with primary antibodies. Next day, sections were incubated with Alexa555 or Alexa 488 (Molecular Probes)-conjugated secondary antibodies and then briefly with bisbenzimide (Sigma-Aldrich) for nuclear counterstaining.

PMMA micropatterning, characterization and sterilization

Goodfellow Ltd. (UK) supplied PMMA sheets (125 µm thick). The Nanolithography Laboratory of the Institute of Microelectronics of Barcelona (IMB) - National Center of Microelectronics (CNM) CSIC prepared Ln2PMMA substrates as a service. Micropatterning consist in linear grooves of 1µm deep/tall and 2µm wide, introduced by nano-imprinting lithography (NIL) and characterized as previously described [14,60]. For cell culture, Ln2PMMA substrates were cut to fit in 60 mm cell culture dishes or 24 multi-well culture plates, sonicated for 10 minutes in sterile water, sterilized in 70% ethanol for 15-20 min, rinsed with sterile water for 20 min, left dry and then used uncoated. We used borosilicate glass cover slips as control substrates, since there were no major differences

in cell morphology and expression of differentiation markers between no patterned PMMA, glass and culture plastic [14].

Immunofluorescence

Cells were fixed in 4% PFA in 0,1M phosphate buffer (pH of 7.2) for 20'. Then, samples were transferred to a new multi-well plate, washed with PBS, 3 times for 5', and blocked for 2h using phosphate buffered saline (PBS) with 3% normal serum (horse and/or goat, Gibco), 0.05% Triton (Sigma-Aldrich), and 0.2M glycine. Then, samples were washed 3 times with PBST (PBS + 0.05% triton) and incubated with primary antibodies overnight at 4ºC with incubation buffer (PBST + 1% normal serum) (listed in Table 1). The next day, samples were washed with PBST (5' x4) and incubated for 2h at room temperature in their appropriate anti-mouse, anti-rabbit or anti-goat Alexa488, Alexa555, or Alexa 649-conjugated secondary antibody (1:1000, Life Technologies). Then, samples were washed with PBST x2 and incubated 15' with Hoechst 33342 (1 µl/mL, life technologies, 1:20000) in PBS, to counterstain cell nuclei. Lastly, samples were washed with PBS, 5' x2, and mounted with in-house Mowiol preparation (Calbiochem, standard protocol). Antibodies dilutions used are listed below.

Primary antibody	**Dilution**	**Reference**	**Molecule and Cell type marker**
Rabbit anti glial fibrillary acidic protein (GFAP)	1:3000	DakoCytomation - Z0334	Intermediate filament, mature astrocyte marker
Rabbit anti NG2	1:600	Millipore - AB5320	Proteoglycan, OPC marker
Rabbit anti Pax6	1:500	Abcam - ab195045	Transcription factor, RG marker
Mouse anti Pax6	1: 500	Santa Cruz - sc-81649	Transcription factor, RG marker
Rabbit anti Sox2	1:3000	Abcam - ab97959	Transcription factor, general stem cell marker
Rabbit anti GSX2	1:500	Thermofisher - 15504202	Transcription factor, Tripotential intermediate progenitor
Mouse anti Nestin	1:3500	BD Pharmigen - 556309	Intermediate filament, RG / immature astrocyte marker
Rabbit anti Ki67	1:500	Abcam – ab15580	No-histone protein, cell cycle marker.
Rabbit anti PH3	1:500	Millipore - 6570	Histone protein, mitosis marker.
Mouse anti Lamin A/C	1:3000	Invitrogen – 14-9847-82	Ubiquitous, nuclear lamina
Rabbit anti Lamin B1	1:3000	Abcam - ab16048	Ubiquitous, nuclear lamina

Rabbit anti YAP/TAZ	1:1000	Cell Signaling - 8418	Transcription factor, ubiquitous, transcription factor
Rabbit anti β-Catenin	1:3000	Abgent – AX10009	Key downstream component (protein) of the canonical Wnt signaling pathway.
Rabbit anti β-Catenin	1:3000	Abgent – AX10009	Key downstream component (protein) of the canonical Wnt signaling pathway.

Image processing

Cell nuclei segmentation

For image acquisition, we used an LSM 880 spectral confocal microscope (Carl Zeiss, Germany) and Plan-Apochromat 40x/1.3 Oil DIC UV-IR M27 objective. In a reduced number of experimental conditions, we also used 25x and 63x objectives. Images were mounted with the ZEN (blue edition) software to obtain projections. We adjusted the number of optical confocal sections depending on the experiment and markers. For each marker, the same settings for acquisition and projection were used for all the experiments. A range of six to nine images from two to four different samples were used for each study. Images were randomly taken at different sample areas while avoiding those of high cell confluence (middle of the sample). In these areas, intercellular interactions overcome mechanical signals from In2PMMA substrate and cells tend to differentiate into astrocytes, as in control substrate [15].

We employed a custom-designed, high-throughput image analysis algorithm developed in MATLAB to extract cellular and nuclear parameters from each image. This allowed us to simultaneous correlate lineage markers with nuclei morphology at the single-cell level. Nuclei segmentation was performed in z-stack orthogonal maximum projections (cell-lineage assignments) or from average projection (intensity fluorescence assays), as we found no significant differences between both types of analysis (**Figure S3**).

Our custom-designed algorithm allowed for semiautomatic processing of immunofluorescence images through the application of specific functions for each wavelength channel. These functions implement advanced segmentation methods combining simple thresholding with more refined techniques such as a modified version of the top-hat algorithm [61]. Segmented pixels in the blue channel (Hoechst staining) were used for the extraction of the nucleus perimeter, area, and eccentricity. Eccentricity (*E*) is the ratio of the distance between the foci of the ellipse that has the same second-moments as the region (nucleus) and its major axis length. It is a non-dimensional

measure that indicates the range of nuclear shape from circular (*E*=0) to a linear segment (*E*=1) shape. Total nuclei per image was also considered to detect correlations between cell density with their morphological features.

When a nucleus is segmented, the algorithm extracts the total intensity within the nuclear region, as well as within the surrounding (perinuclear) region that has the same area as the original nucleus, as proposed [32] for the analysis of cytosolic to nuclear protein translocation. We used this approach to calculate nuclear and cytoplasmic intensity ratios in transcriptional cofactors analysis (YAP/TAZ and β-catenin) (**Figure S4A**) and nuclear fluorescence intensity of lamin A-C and lamin B1 nuclear proteins (**Figure S4B**). Intensity extraction from two different markers within the same nucleus required specific attention to avoid fluorescence overlapping and the use of the same segmentation in both channels. This step was manually performed and revised.

Figure S5 illustrates the nuclei analysis app developed for the image analysis with examples of the main features used. We included different microscopes to the MATLAB algorithm to be able to combine data from different sources (**Table S3**).

To optimize nuclear detection, we evaluated various nuclear staining methods to identify the one that maximized the number of detectable nuclei under the program's default parameters, avoiding time-intensive parameter adjustments. Lamin B1, a nuclear intermediate filament commonly used in nuclear morphology studies [62], was compared to Hoechst staining, a frequently used nuclear counterstain in immunostaining protocols. We assessed which stain enabled more effective nuclear segmentation (**Figure S6A**). Our results showed that Hoechst staining facilitated the segmentation of 16% more nuclei than lamin B1 in control samples, and 18% more in In2PMMA substrates, based on a reference detection rate of 50% (**Figure S6B**). Importantly, there were no significant differences in area or eccentricity measurements for individual nuclei between the two staining methods (**Figure S6C**). Therefore, Hoechst was selected as the primary nuclear stain for all segmentation analyses.

Nuclear morphology data obtained from in vivo images was obtained using the freehand tool of ImageJ Fiji Software. For analysis, individual images were selected, ranging from a single slice to a maximum projection of three consecutive slices from the image stack. The usage of automated segmentation methods was challenging and nuclei were not well segmented. Cell density associated to in vivo images was manually calculated. Moreover, images with different brain zones, as well, VZ, SVZ and IZ, cell density was assigned per zone instead of per picture.

Logistic Regression Model Construction for RG Markers

Model Overview

To investigate the relationship between nuclear morphology parameters and the expression of radial glia (RG) cell markers, we constructed a logistic regression model in R (R Core Team, Vienna, Austria), a statistical computing environment. The model analyzes data obtained from confocal images of primary mouse cortical astrocyte cultures grown for 3 days in vitro (3DIV) on either control or In2PMMA substrates, with cells immunostained using specific markers as previously described.

Image Variable Definition

For model inputs, we defined a covariate vector comprising:

- Nuclear morphology parameters: Area (μm², as a measure of size) and eccentricity (dimensionless, as a measure of shape).
- Cell density: Calculated as the total nuclei count per area of the confocal image.
- Substrate type: control or In2PMMA.

The dataset was obtained from 15 independent immunofluorescence assays on glial cells cultured on both substrate types, producing a sample of 3,855 nuclei. To account for cell density variability, we captured 7-12 images per substrate condition from areas representing low, medium, and high confluence levels.

Response Variable Definition

The binary response variable classifies nuclei as RG or Non-RG based on the presence of RG markers, which vary according to cell lineage stages. A nucleus was labeled as RG if it expressed Pax6+, either alone or combined with nestin+/-, GFAP+/-, or Sox2+/-, or if it expressed Sox2+ combined with nestin+. Non-RG cells were defined as those either double-negative for Pax6/nestin, Pax6/GFAP, or Sox2/nestin, or positive for lineage-committed markers (e.g., NG2+, Gsx2+, or Pax6-/GFAP+). Cells lacking specific marker expression were labeled as undetermined cells. Markers combination and its category are listed below.

RG **N=374**	**Non-RG** **N=786**	**Undetermined** **N=1295**
Pax6+/Nestin+	Pax6-/Nestin-	Nestin-/Sox2+
Pax6+/Nestin-	Pax6-/GFAP+	Pax6-/Sox2+

Pax6+/Sox2+	Pax6-/Sox2-	Nestin+/--
Pax6+/Sox2-	Nestin-/Sox2-	Sox2+/--
Nestin+/Sox2+	Nestin-/NG2+	GFAP+/--
Pax6+/GFAP+	Nestin+/NG2+	Nestin+/NG2-
Pax6+/GFAP-	Nestin-/GFAP-	Nestin+/GFAP+
Pax6+/--	Nestin-/GFAP+	Nestin+/GFAP-
	Pax6-/GFAP-	Nestin+/Sox2-
	NG2+/--	Nestin+/Pax6-
	Gsx2+/--	

Logistic Regression Model Construction for RG Markers

We implemented a Generalized Linear Model (GLM) with a logit link to accommodate non-normal data and to predict the probability of RG marker expression based on morphological parameters. The logit function transforms the linear predictor (a weighted sum of predictor variables) into the probability of a binary outcome.

The linear prediction equation for RG (response *y* = 1) given the morphological predictor – eccentricity (*E*), area (*A*), and cell density (*D*) - is defined as follows:

$$P(RG) = \frac{\exp(\beta_0 + \boldsymbol{g}(\boldsymbol{E}, \boldsymbol{A}, \boldsymbol{D}))}{1 + exp(\beta_0 + \boldsymbol{g}(\boldsymbol{E}, \boldsymbol{A}, \boldsymbol{D}))}$$

Due to the nature of our data and the type of response, we used the function logit link to define the relationship between the linear and the expected value of the response variable. The logit link function maps the linear predictor to the odds of success in binomial distributions, as shown in the following equation:

$$logit\big(P(RG)\big) = \beta_0 + \boldsymbol{g}(\boldsymbol{E}, \boldsymbol{A}, \boldsymbol{D}) = (\mathrm{poly}(\mathbf{E}, \mathrm{k_E}) + \mathrm{poly}(\mathbf{A}, \mathrm{k_A})) * (\mathbf{Material} + \mathbf{D})$$

Where *g(E, A, D)* represents polynomial expansions and interaction terms and *K* terms representing the polynomial degree.

Selected model

The model selection process was based on maximum likelihood estimation (MLE) and minimized Akaike Information Criterion (AIC) for model fit and complexity balance. Terms significant at the $p < 0.05$ level were retained in the final model. Most non-significant terms were eliminated; however, terms relevant only in specific substrate interactions were retained, even if they were non-significant in the counterpart substrate. The

following table summarizes the model coefficients, standard errors, z-values, and p-values.

Term	Estimate	Std. Error	z value	p-value
(Intercept)	-5.82E+03	7.62E+02	-7.634	0
Ln2PMMA	-9.45E+02	5.66E+02	-1.669	0.095
Area	1.51E+02	2.58E+01	5.829	0
Area^2	-1.05E+00	2.22E-01	-4.755	0
Area^3	1.81E-03	5.49E-04	3.296	0.001
Control * Eccentricity^3	-2.31E+02	8.84E+02	-0.261	0.794
Ln2PMMA * Eccentricity^3	2.57E+03	7.32E+02	3.509	0
Ln2PMMA * Area	-7.33E+00	4.74E+00	-1.546	0.122
Eccentricity^2 * cell density	5.15E+00	2.49E+00	2.068	0.039
Eccentricity^3 * cell density^2	-2.75E-03	1.50E-03	-1.834	0.067
Area * cell density	-1.46E-01	4.13E-02	-3.522	0
Area * cell density^2	8.80E-05	2.37E-05	3.722	0
Area^2 * cell density	8.91E-04	2.78E-04	3.2	0.001
Area^2 * cell density^2	-6.22E-07	1.84E-07	-3.384	0.001

Substrate-specific terms allow for distinct RG classifications by substrate type (control and ln2PMMA), introducing different interaction pathways. The two primary logit equations are **eq.1** for control and **eq.2** for ln2PMMA.

The expression *logit (…)* indicated the application of the linear predictor to the associated probability to the response $y=1$, using the variables X in control or ln2PMMA. β corresponds to estimated coefficients, A corresponds to area, E to eccentricity and D to cell density. Specific terms depending on substrate were indicated as C for control and Ln2 for ln2PMMA.

Quadratic and cubic terms reflect complex relationships among nuclear morphology features and RG marker expression, with the direction and significance of each effect indicated by the z-value and p-value. We guided the model by a stepwise model selection and refinement based on AIC, ensuring model parsimony without compromising essential predictive interactions. To assess classification performance, we computed the AUC for Receiver Operating Characteristic (ROC) curves (**Figure 2 Main text**).

Describing the equation and model validation

To identify substrate-conditioned variables, we calculated the odds ratio based on equations (1) and (2). The odds ratio serves as a measure of association between

conditions or variables, allowing us to compare the impact of substrates on nuclear morphology. The odds ratio for substrates is calculated as follows:

$$Odds\ ratio = \frac{Odds\ (Ln2PMMA)}{Odds\ (Control)} = \frac{\exp(\beta_{0Ln2} + \beta_{E^3Ln2}\mathrm{E}^3 + \beta_{ALn2}A)}{\exp(\beta_{E^3C}\mathrm{E}^3)}$$

For streamlined interpretation and application, we converted this to the *log-odds ratio*. This transformation allowed us to address two critical questions:

1. Quantifying substrate effects: We determined the proportion of change in nuclear morphology driven by ln2PMMA compared to control conditions.
2. Threshold determination: At a log-odds ratio of 0, the threshold for substrate-induced versus intrinsic nuclear deformation is established, delineating an intrinsic mechanical property threshold essential for RG morphology in glial nuclei.

The log-odds ratio calculation was applied directly to nuclear data.

Model Validation Procedure

Model validation was conducted using independent datasets from glial cells cultured for 3DIV in two biological samples and immunostained for RG markers (nestin/GFAP and Pax6/nestin). The model-predicted counts of RG cells were compared to experimentally observed counts.

Dataset requirements and model application workflow

Before applying the model, new data were assessed to ensure they fell within the established parameter range of the training data. Any extrapolated data points outside this range were flagged and excluded to maintain model reliability.

The model application process included two main approaches:

1. Prediction of RG Cell Percentages: For each nucleus, fitted probabilities (0 to 1 on the x-axis) were generated and represented in density plots. Percentages of nucleus with fitted probability is over thresholds 1/2 (50%) were calculatedto evaluate predictive accuracy. This only can be applied to non-extrapolated data.
2. Log-Odds Ratio and Mechanical Factor Threshold: To identify nuclei conforming to RG-associated morphology, we examined the *log-odds ratio* values. This

threshold, denoted as F(0), represents the mechanical factor required for RG morphology. Surface plots were generated to visualize this threshold across area (x-axis) and eccentricity (y-axis), and calculated the proportions of data above each threshold. This qualitative approach is particularly useful for analyzing nuclei that do not meet all model criteria—such as samples with high cell density, including hRG and hNeuron cultures, brain slices, hiPSCs, and heNPCs. Although not all samples exhibit extrapolated data, applying the log-odds ratio exclusively allows us to maximize data use from the experimental set while avoiding potential bias from extrapolated values.

Code Availability and Model Scripts

The primary scripts for constructing, applying, and visualizing the RGM model are available at https://github.com/PepPau/RGM-model-main-scripts.git.

Publicly available single-cell transcriptomics data analysis

To analyze mRNA expression at different developmental stages, we used mouse cerebral cortex single-cell transcriptomics data from a previous study by Di Bella et al.[31] deposited on the GEO database with accession number GSE153162. We used SCANPY [63] to apply quality control filters based on the distribution of counts and genes found on each dataset. We discarded all cells with less than 500 UMIs or more than 50000, all those with less than 800 detected genes and those with more than 7000, and all the cells with more than 15% of mitochondrial content. In total we retained 81792 out of the initial 82415 cells. Subsequently, we discarded an additional 2431 cells that had been identified as doublets by the scrublet package [64]. To retain only cells from relevant developmental stages for our study, we discarded all the cells from E10, E11 and E12. After this selection, we were left with 67961 cells. We then normalized the data using the normalize_total function from SCANPY with a target of 10000 counts per cell, and then we log-transformed the data. We applied dimensionality reduction keeping the first 10 principal components, clustered the data using the Louvain algorithm for community detection (Levine et al., 2015) (r=0.2) and selected clusters expressing RG-astrocyte lineage markers (Sox2, Pax6, Hes5) and no expression of neuronal (Neurod2, Tubb3, Neurod6, Meg3). We applied again principal component analysis (PCA) on the 14469 selected cells, clustered them on the space of the first 11 principal components and removed those clusters expressing neuronal or oligodendrocyte (Olig1, Olig2, Pdgfra) lineage makers, except for a cluster which expressed both Olig1 and mature astrocyte markers (Aqp4, Slc1a2). After this selection, we retained 9343 that we confidently

labeled as RG-astrocyte lineage cells, on which we examined the expression of our proteins of interest.

Calcium Imaging

To record intracellular calcium levels in glial cultures, samples at 3-4 days in vitro (DIV) were positioned in a microfluidic chamber (Open Diamond Bath Imaging Chamber for Round Coverslips; Warner Instruments). Samples were loaded with the calcium-sensitive dye Oregon Green BAPTA-1 AM (OGB-1 AM, Life Technologies) at a concentration of 10 µM for 30 minutes at 37°C and 5% CO_2. The OGB-1 AM working solution was prepared in EM to prevent cell detachment, which was observed with PBS.

For calcium imaging, the bath solution contained 140 mM NaCl, 5.4 mM KCl, 1 mM $MgCl_2$, 10 mM HEPES, and 10 mM glucose, adjusted to pH 7.4. The solution was used under both calcium-free and calcium-containing conditions, with 2 mM $CaCl_2$ added where specified. Intracellular Ca^{2+} activity was recorded over 10 minutes, divided into two phases: an initial 2-minute calcium-free stage to establish baseline activity, followed by 2 mM $CaCl_2$ supplementation.

Imaging was performed on an Olympus IX71 inverted microscope using an XLUMPLFLN 20XW water immersion objective (20x/1, Olympus). OGB-1 AM was excited at 488 nm (50 ms exposure) using a Polychrome V light source (Till Photonics) with a Xenon Short-Arc lamp (Ushio), alongside a 505 nm dichroic beam splitter (Chroma Technology). Emission at 510 nm was filtered with a D535/40 nm emission filter (Chroma Technology) and captured by a C9100-13 EM-CCD camera (Hamamatsu). The emission spectrum shifts in amplitude and peak wavelength upon Ca^{2+} binding, with fluorescence intensity changes indicating free calcium levels, which are quantitatively estimated using the EM-CCD camera. Images were acquired at 1-second intervals at room temperature.

After recording, a marker was drawn on the back of the sample at the recorded area. Samples were subsequently washed and incubated in EM at 37°C for 30-60 minutes before fixation and preparation for immunocytochemistry (as described above). For each substrate, eight samples were immunolabeled with Pax6 and nestin markers, although three samples experienced cell loss due to handling, and alignment issues with the recorded area prevented analysis in one sample. Imaging was conducted on a Zeiss LSM 880 spectral confocal microscope with an LD LCI Plan-Apochromat 25x/0.8 Imm Korr DIC M27 objective. Alignment challenges between the 20x objective used in calcium recordings and confocal objectives necessitated a 0.7x zoom adjustment to match focal planes. Both calcium and confocal images required orientation corrections, and confocal

images from In2PMMA samples required flipping due to cell orientation (face-up) (**Figure S7A**).

Calcium Imaging analysis

Calcium signal data was analyzed with a custom-designed MATLAB algorithm to extract nuclear calcium signals in a defined ROI. ImageJ snapshots of calcium signals were co-localized with immunolabeled images to correlate nuclear morphology, expression markers, and calcium signals. A representative cross-correlation is shown in **Figure S7B**.

To quantify relative intracellular calcium levels (fluorescence intensity), background fluorescence was subtracted from each cell's calcium signal at each time point. Background values were obtained by averaging 10 ROIs from cell-free areas and analyzing each time point. The background was carefully examined to avoid artifacts (**Figure S8**).

Calcium activity patterns were smoothed using a Savitzky-Golay filter (polynomial order = 2, window size = 6) in Origin Pro v9 (OriginLab, Northampton, MA, USA). **Figure S9** illustrates the raw versus filtered signal. To minimize artifacts, the first 50 frames were excluded, and the signal-to-baseline ratio (SBR) or $\Delta F/F_0$ was calculated using the following formulas:

- $F_0 = \frac{\sum_{i=1}^{50} F_{Baseline}(t)_i}{50}$
- $\frac{\Delta F}{F_0} = \frac{F_i(t) - F_0}{F_0}$

To perform analysis and plots we applied an increase of 100% to the resultant signal, i.e. % = $\frac{\Delta F}{F_0}$ x100.

Statistical analysis

Statistical analyzes were performed using IBM SPSS (Version 26), GraphPad Prism version 8.0, R Core Team (2021), RStudio and R: A language and environment for statistical computing (R Foundation for Statistical Computing, Vienna, Austria). We performed the normality test by default and different post-hoc tests depending on the nature of the data. For two sample comparisons we used t-test or Mann-Whitney. For three or more sample comparisons we used one-way or two-way analysis of variance (ANOVA, with Tukey adjustment) or Kruskal-Wallis with multiple comparison test (with

Benjamini-Yekutieli and Krieger FDR correction). To determine differences between populations we performed chi-square tests for 4 groups or multiple regression approach in contingency tables for more than 4 groups adapted from [65]. To demonstrate statistical significance, we deemed it sufficient to utilize thresholds such as $p < 0.05$ and $p < 0.01$. While we frequently observed values lower than $p = 0.001$ in numerous instances, we found that adopting a threshold of $p < 0.01$ was satisfactory for identifying meaningful biological distinctions.

BIBLIOGRAPHY

1. Chighizola, M., Dini, T., Lenardi, C., Milani, P., Podestà, A., and Schulte, C. (2019). Mechanotransduction in neuronal cell development and functioning. Biophys Rev *11*, 701-720. 10.1007/s12551-019-00587-2.
2. Fujita, I., Shitamukai, A., Kusumoto, F., Mase, S., Suetsugu, T., Omori, A., Kato, K., Abe, T., Shioi, G., Konno, D., and Matsuzaki, F. (2020). Endfoot regeneration restricts radial glial state and prevents translocation into the outer subventricular zone in early mammalian brain development. Nat Cell Biol *22*, 26-37. 10.1038/s41556-019-0436-9.
3. Ferent, J., Zaidi, D., and Francis, F. (2020). Extracellular Control of Radial Glia Proliferation and Scaffolding During Cortical Development and Pathology. Front Cell Dev Biol *8*, 578341. 10.3389/fcell.2020.578341.
4. Merkle, F.T., and Alvarez-Buylla, A. (2006). Neural stem cells in mammalian development. Curr Opin Cell Biol *18*, 704-709. 10.1016/j.ceb.2006.09.008.
5. Malatesta, P., and Götz, M. (2013). Radial glia - from boring cables to stem cell stars. Development *140*, 483-486. 10.1242/dev.085852.
6. Mihalas, A.B., and Hevner, R.F. (2017). Control of Neuronal Development by T-Box Genes in the Brain. Curr Top Dev Biol *122*, 279-312. 10.1016/bs.ctdb.2016.08.001.
7. Nishiyama, A., Boshans, L., Goncalves, C.M., Wegrzyn, J., and Patel, K.D. (2016). Lineage, fate, and fate potential of NG2-glia. Brain Res *1638*, 116-128. 10.1016/j.brainres.2015.08.013.
8. Zhang, Y., Liu, G., Guo, T., Liang, X.G., Du, H., Yang, L., Bhaduri, A., Li, X., Xu, Z., Zhang, Z., et al. (2020). Cortical Neural Stem Cell Lineage Progression Is Regulated by Extrinsic Signaling Molecule Sonic Hedgehog. Cell Rep *30*, 4490-4504.e4494. 10.1016/j.celrep.2020.03.027.
9. Hunter, K.E., and Hatten, M.E. (1995). Radial glial cell transformation to astrocytes is bidirectional: regulation by a diffusible factor in embryonic forebrain. Proc Natl Acad Sci U S A *92*, 2061-2065. 10.1073/pnas.92.6.2061.
10. Zamboni, M., Llorens-Bobadilla, E., Magnusson, J.P., and Frisén, J. (2020). A Widespread Neurogenic Potential of Neocortical Astrocytes Is Induced by Injury. Cell Stem Cell *27*, 605-617.e605. 10.1016/j.stem.2020.07.006.
11. Yang, J.L., Fan, H., Fu, F.F., Guo, B.L., Huang, Y., Sun, L., Wang, W.T., Xing, J.L., Hu, X.T., Ding, Y.Q., et al. (2023). Transient neurogenesis in ischemic cortex from Sox2. Neural Regen Res *18*, 1521-1526. 10.4103/1673-5374.357910.
12. Ozgun, A., Lomboni, D., Arnott, H., Staines, W.A., Woulfe, J., and Variola, F. (2022). Biomaterials-based strategies for. Biomater Sci *10*, 1134-1165. 10.1039/d1bm01361k.
13. Castillo Ransanz, L., Van Altena, P.F.J., Heine, V.M., and Accardo, A. (2022). Engineered cell culture microenvironments for mechanobiology studies of brain neural cells. Front Bioeng Biotechnol *10*, 1096054. 10.3389/fbioe.2022.1096054.
14. Mattotti, M., Alvarez, Z., Ortega, J.A., Planell, J.A., Engel, E., and Alcantara, S. (2012). Inducing functional radial glia-like progenitors from cortical astrocyte cultures using micropatterned PMMA. Biomaterials *33*, 1759-1770. 10.1016/j.biomaterials.2011.10.086.
15. Alvarez, Z., Sena, E., Mattotti, M., Engel, E., and Alcantara, S. (2014). An efficient and reproducible method to culture Bergmann and cortical radial glia using textured PMMA. Journal of Neuroscience Methods *232*, 93-101. 10.1016/j.jneumeth.2014.05.011.
16. Mattotti, M., Alvarez, Z., Delgado, L., Mateos-Timoneda, M.A., Aparicio, C., Planell, J.A., Alcantara, S., and Engel, E. (2017). Differential neuronal and glial behavior on flat and micro patterned chitosan films. Colloids and Surfaces B-Biointerfaces *158*, 569-577. 10.1016/j.colsurfb.2017.07.045.

17. Kumar, S. (2014). Cellular mechanotransduction: stiffness does matter. Nat Mater *13*, 918-920. 10.1038/nmat4094.
18. Kirby, T.J., and Lammerding, J. (2018). Emerging views of the nucleus as a cellular mechanosensor. Nat Cell Biol *20*, 373-381. 10.1038/s41556-018-0038-y.
19. Kalukula, Y., Stephens, A.D., Lammerding, J., and Gabriele, S. (2022). Mechanics and functional consequences of nuclear deformations. Nat Rev Mol Cell Biol *23*, 583-602. 10.1038/s41580-022-00480-z.
20. Martino, F., Perestrelo, A.R., Vinarský, V., Pagliari, S., and Forte, G. (2018). Cellular Mechanotransduction: From Tension to Function. Front Physiol *9*, 824. 10.3389/fphys.2018.00824.
21. Park, M.G., Jang, H., Lee, S.H., and Lee, C.J. (2017). Flow Shear Stress Enhances the Proliferative Potential of Cultured Radial Glial Cells Possibly Via an Activation of Mechanosensitive Calcium Channel. Exp Neurobiol *26*, 71-81. 10.5607/en.2017.26.2.71.
22. Chi, S., Cui, Y., Wang, H., Jiang, J., Zhang, T., Sun, S., Zhou, Z., Zhong, Y., and Xiao, B. (2022). Astrocytic Piezo1-mediated mechanotransduction determines adult neurogenesis and cognitive functions. Neuron *110*, 2984-2999.e2988. 10.1016/j.neuron.2022.07.010.
23. Shao, W., Yang, J., He, M., Yu, X.Y., Lee, C.H., Yang, Z., Joyner, A.L., Anderson, K.V., Zhang, J., Tsou, M.B., et al. (2020). Centrosome anchoring regulates progenitor properties and cortical formation. Nature *580*, 106-112. 10.1038/s41586-020-2139-6.
24. Yanakieva, I., Erzberger, A., Matejčić, M., Modes, C.D., and Norden, C. (2019). Cell and tissue morphology determine actin-dependent nuclear migration mechanisms in neuroepithelia. J Cell Biol *218*, 3272-3289. 10.1083/jcb.201901077.
25. Duran, I., Pombo, J., Sun, B., Gallage, S., Kudo, H., McHugh, D., Bousset, L., Barragan Avila, J.E., Forlano, R., Manousou, P., et al. (2024). Detection of senescence using machine learning algorithms based on nuclear features. Nat Commun *15*, 1041. 10.1038/s41467-024-45421-w.
26. Niethammer, P. (2021). Components and Mechanisms of Nuclear Mechanotransduction. Annu Rev Cell Dev Biol *37*, 233-256. 10.1146/annurev-cellbio-120319-030049.
27. Ndiaye, A.B., Koenderink, G.H., and Shemesh, M. (2022). Intermediate Filaments in Cellular Mechanoresponsiveness: Mediating Cytoskeletal Crosstalk From Membrane to Nucleus and Back. Front Cell Dev Biol *10*, 882037. 10.3389/fcell.2022.882037.
28. Saka, Y., Lhoussaine, C., Kuttler, C., Ullner, E., and Thiel, M. (2011). Theoretical basis of the community effect in development. BMC Syst Biol *5*, 54. 10.1186/1752-0509-5-54.
29. Mestres, I., Houtman, J., Calegari, F., and Toda, T. (2022). A Nuclear Belt Fastens on Neural Cell Fate. Cells *11*. 10.3390/cells11111761.
30. Wang, M., Ivanovska, I., Vashisth, M., and Discher, D.E. (2022). Nuclear mechanoprotection: From tissue atlases as blueprints to distinctive regulation of nuclear lamins. APL Bioeng *6*, 021504. 10.1063/5.0080392.
31. Di Bella, D.J., Habibi, E., Stickels, R.R., Scalia, G., Brown, J., Yadollahpour, P., Yang, S.M., Abbate, C., Biancalani, T., Macosko, E.Z., et al. (2021). Molecular logic of cellular diversification in the mouse cerebral cortex. Nature *595*, 554-559. 10.1038/s41586-021-03670-5.
32. Elosegui-Artola, A., Andreu, I., Beedle, A.E.M., Lezamiz, A., Uroz, M., Kosmalska, A.J., Oria, R., Kechagia, J.Z., Rico-Lastres, P., Le Roux, A.L., et al. (2017). Force Triggers YAP Nuclear Entry by Regulating Transport across Nuclear Pores. Cell *171*, 1397-1410.e1314. 10.1016/j.cell.2017.10.008.
33. Wagh, K., Garcia, D.A., and Upadhyaya, A. (2021). Phase separation in transcription factor dynamics and chromatin organization. Curr Opin Struct Biol *71*, 148-155. 10.1016/j.sbi.2021.06.009.

34. Sen, B., Xie, Z., Howard, S., Styner, M., van Wijnen, A.J., Uzer, G., and Rubin, J. (2022). Mechanically Induced Nuclear Shuttling of β-Catenin Requires Co-transfer of Actin. Stem Cells *40*, 423-434. 10.1093/stmcls/sxac006.
35. Wrobel, C.N., Mutch, C.A., Swaminathan, S., Taketo, M.M., and Chenn, A. (2007). Persistent expression of stabilized beta-catenin delays maturation of radial glial cells into intermediate progenitors. Dev Biol *309*, 285-297. 10.1016/j.ydbio.2007.07.013.
36. Gao, J., Liao, Y., Qiu, M., and Shen, W. (2021). Wnt/β-Catenin Signaling in Neural Stem Cell Homeostasis and Neurological Diseases. Neuroscientist *27*, 58-72. 10.1177/1073858420914509.
37. Rosenbloom, A.B., Tarczyński, M., Lam, N., Kane, R.S., Bugaj, L.J., and Schaffer, D.V. (2020). β-Catenin signaling dynamics regulate cell fate in differentiating neural stem cells. Proc Natl Acad Sci U S A *117*, 28828-28837. 10.1073/pnas.2008509117.
38. Lavado, A., Gangwar, R., Paré, J., Wan, S., Fan, Y., and Cao, X. (2021). YAP/TAZ maintain the proliferative capacity and structural organization of radial glial cells during brain development. Dev Biol *480*, 39-49. 10.1016/j.ydbio.2021.08.010.
39. Weissman, T.A., Riquelme, P.A., Ivic, L., Flint, A.C., and Kriegstein, A.R. (2004). Calcium waves propagate through radial glial cells and modulate proliferation in the developing neocortex. Neuron *43*, 647-661. 10.1016/j.neuron.2004.08.015.
40. Rash, B.G., Ackman, J.B., and Rakic, P. (2016). Bidirectional radial Ca(2+) activity regulates neurogenesis and migration during early cortical column formation. Sci Adv *2*, e1501733. 10.1126/sciadv.1501733.
41. Arjun McKinney, A., Petrova, R., and Panagiotakos, G. (2022). Calcium and activity-dependent signaling in the developing cerebral cortex. Development *149*. 10.1242/dev.198853.
42. Ortega, J.A., Sirois, C.L., Memi, F., Glidden, N., and Zecevic, N. (2017). Oxygen Levels Regulate the Development of Human Cortical Radial Glia Cells. Cereb Cortex *27*, 3736-3751. 10.1093/cercor/bhw194.
43. Ortega, J.A., Radonjić, N.V., and Zecevic, N. (2013). Sonic hedgehog promotes generation and maintenance of human forebrain Olig2 progenitors. Front Cell Neurosci *7*, 254. 10.3389/fncel.2013.00254.
44. Imamura, O., Pagès, G., Pouysségur, J., Endo, S., and Takishima, K. (2010). ERK1 and ERK2 are required for radial glial maintenance and cortical lamination. Genes Cells *15*, 1072-1088. 10.1111/j.1365-2443.2010.01444.x.
45. Sanchez-Camacho, C., Alberto Ortega, J., Ocana, I., Alcantara, S., and Bovolenta, P. (2011). Appropriate Bmp7 Levels are Required for the Differentiation of Midline Guidepost Cells Involved in Corpus Callosum Formation. Developmental Neurobiology *71*, 337-350. 10.1002/dneu.20865.
46. Dupont, S., and Wickström, S.A. (2022). Mechanical regulation of chromatin and transcription. Nat Rev Genet *23*, 624-643. 10.1038/s41576-022-00493-6.
47. Ochi, S., Manabe, S., Kikkawa, T., and Osumi, N. (2022). Thirty Years' History since the Discovery of Pax6: From Central Nervous System Development to Neurodevelopmental Disorders. Int J Mol Sci *23*. 10.3390/ijms23116115.
48. Yuste, R., Hawrylycz, M., Aalling, N., Aguilar-Valles, A., Arendt, D., Armañanzas, R., Ascoli, G.A., Bielza, C., Bokharaie, V., Bergmann, T.B., et al. (2020). A community-based transcriptomics classification and nomenclature of neocortical cell types. Nat Neurosci *23*, 1456-1468. 10.1038/s41593-020-0685-8.
49. Miranda-Negrón, Y., and García-Arrarás, J.E. (2022). Radial glia and radial glia-like cells: Their role in neurogenesis and regeneration. Front Neurosci *16*, 1006037. 10.3389/fnins.2022.1006037.
50. Eze, U.C., Bhaduri, A., Haeussler, M., Nowakowski, T.J., and Kriegstein, A.R. (2021). Single-cell atlas of early human brain development highlights heterogeneity of human

neuroepithelial cells and early radial glia. Nat Neurosci *24*, 584-594. 10.1038/s41593-020-00794-1.

51. Mattiazzi Usaj, M., Yeung, C.H.L., Friesen, H., Boone, C., and Andrews, B.J. (2021). Single-cell image analysis to explore cell-to-cell heterogeneity in isogenic populations. Cell Syst *12*, 608-621. 10.1016/j.cels.2021.05.010.
52. Smith, K., Piccinini, F., Balassa, T., Koos, K., Danka, T., Azizpour, H., and Horvath, P. (2018). Phenotypic Image Analysis Software Tools for Exploring and Understanding Big Image Data from Cell-Based Assays. Cell Syst *6*, 636-653. 10.1016/j.cels.2018.06.001.
53. Rammensee, S., Kang, M.S., Georgiou, K., Kumar, S., and Schaffer, D.V. (2017). Dynamics of Mechanosensitive Neural Stem Cell Differentiation. Stem Cells *35*, 497-506. 10.1002/stem.2489.
54. Erdemir, A., Mulugeta, L., Ku, J.P., Drach, A., Horner, M., Morrison, T.M., Peng, G.C.Y., Vadigepalli, R., Lytton, W.W., and Myers, J.G. (2020). Credible practice of modeling and simulation in healthcare: ten rules from a multidisciplinary perspective. J Transl Med *18*, 369. 10.1186/s12967-020-02540-4.
55. Gurdon, J.B. (1988). A community effect in animal development. Nature *336*, 772-774. 10.1038/336772a0.
56. Stone, M. (1978). Cross-validation: a review. .
57. Vahabikashi, A., Adam, S.A., Medalia, O., and Goldman, R.D. (2022). Nuclear lamins: Structure and function in mechanobiology. APL Bioeng *6*, 011503. 10.1063/5.0082656.
58. Gan, Q., Lee, A., Suzuki, R., Yamagami, T., Stokes, A., Nguyen, B.C., Pleasure, D., Wang, J., Chen, H.W., and Zhou, C.J. (2014). Pax6 mediates ß-catenin signaling for self-renewal and neurogenesis by neocortical radial glial stem cells. Stem Cells *32*, 45-58. 10.1002/stem.1561.
59. Schildge, S., Bohrer, C., Beck, K., and Schachtrup, C. (2013). Isolation and culture of mouse cortical astrocytes. J Vis Exp. 10.3791/50079.
60. Mills, C.A., Martinez, E., Errachid, A., Engel, E., Funes, M., Moormann, C., Wahlbrink, T., Gomila, G., Planell, J., and Samitier, J. (2007). Nanoembossed polymer substrates for biomedical surface interaction studies. J Nanosci Nanotechnol *7*, 4588-4594.
61. Bai, J., Liu, K., Jiang, Y., Ying, K., Zhang, P., and Shao, J. (2008). A two-dimensional CVIB imaging system with a speckle tracking algorithm. Ultrasonics *48*, 394-402. 10.1016/j.ultras.2008.01.010.
62. van Tienen, F.H.J., Lindsey, P.J., Kamps, M.A.F., Krapels, I.P., Ramaekers, F.C.S., Brunner, H.G., van den Wijngaard, A., and Broers, J.L.V. (2019). Assessment of fibroblast nuclear morphology aids interpretation of LMNA variants. Eur J Hum Genet *27*, 389-399. 10.1038/s41431-018-0294-0.
63. Wolf, F.A., Angerer, P., and Theis, F.J. (2018). SCANPY: large-scale single-cell gene expression data analysis. Genome Biol *19*, 15. 10.1186/s13059-017-1382-0.
64. Wolock, S.L., Lopez, R., and Klein, A.M. (2019). Scrublet: Computational Identification of Cell Doublets in Single-Cell Transcriptomic Data. Cell Syst *8*, 281-291.e289. 10.1016/j.cels.2018.11.005.
65. Beasley, T.M., and Schumacker, R.a.E. (1995). Multiple Regression Approach to Analyzing Contingency Tables: Post Hoc and Planned comparison procedures. *The Journal of Experimental Education 64* (*nº 1*), 79-93. http://www.jstor.org/stable/20152474.